J. Fluid Mech. (2010), *vol.* 654, *pp.* 5–34.
doi:10.1017/S0022112010001552

Formation of coherent structures by fluid inertia in three-dimensional laminar flows

Z. POURANSARI[1]†, M. F. M. SPEETJENS[2] AND H. J. H. CLERCX[1]‡

[1]Fluid Dynamics Laboratory, Department of Applied Physics, Eindhoven University of Technology, P.O. Box 513, 5600 MB Eindhoven, The Netherlands

[2]Energy Technology Laboratory, Department of Mechanical Engineering, Eindhoven University of Technology, P.O. Box 513, 5600 MB Eindhoven, The Netherlands

(Received 15 December 2009; revised 24 March 2010; accepted 24 March 2010)

Mixing under laminar flow conditions is key to a wide variety of industrial fluid systems of size extending from micrometres to metres. Profound insight into three-dimensional laminar mixing mechanisms is essential for better understanding of the behaviour of such systems and is in fact imperative for further advancement of (in particular, microscopic) mixing technology. This insight remains limited to date, however. The present study concentrates on a fundamental transport phenomenon relevant to laminar mixing: the formation and interaction of coherent structures in the web of three-dimensional paths of passive tracers due to fluid inertia. Such coherent structures geometrically determine the transport properties of the flow and thus their formation and topological structure are essential to three-dimensional mixing phenomena. The formation of coherent structures, its universal character and its impact upon three-dimensional transport properties is demonstrated by way of experimentally realizable time-periodic model flows. Key result is that fluid inertia induces partial disintegration of coherent structures of the non-inertial limit into chaotic regions and merger of surviving parts into intricate three-dimensional structures. This response to inertial perturbations, though exhibiting great diversity, follows a universal scenario and is therefore believed to reflect an essentially three-dimensional route to chaos. Furthermore, a first outlook towards experimental validation and investigation of the observed dynamics is made.

Key words: chaotic advection, low-Reynolds-numbers flows, nonlinear dynamical systems

1. Introduction

Transport under laminar flow conditions is key to a wide variety of industrial systems of size extending from microns to metres. Examples range from the traditional (and still very relevant) mixing of viscous fluids (Ottino 1989; Aref 2002; Wiggins & Ottino 2004) via compact processing equipment (Jaluria 2003; Sunden & Shah 2007) to rapidly emerging fields as micro-processing equipment (Bertsch *et al.* 2001; Ottino & Wiggins 2004; Stone, Stroock & Ajdari 2004; Nguyen & Wu 2005), lab-on-a-chip

† Present address: Linné Flow Centre, KTH Mechanics, SE-100 44 Stockholm, Sweden
‡ Email address for correspondence: H.J.H.Clercx@tue.nl

applications in molecular analysis (Meagher *et al.* 2008; Weigl, Labarre & Gerlach 2008) and biotechnology (Beebe, Mensing & Walker 2002; Tourovskaia, Figueroa-Masot & Folch 2005). Purposes are equally diverse and range from classical mixing enhancement via thermal homogenization to advanced functionalities as creation of specific gradient fields and targeted delivery of mass in designated flow regions in micro-reactors and lab-on-a-chip systems.

Profound insight into laminar transport, especially in complex three-dimensional unsteady systems, is imperative for further advancement in, particularly, emerging fields as process intensification and micro-fluidics. These areas, even more so than conventional macroscopic applications, rely heavily on accurate knowledge and manipulation of scalar transport (Stone *et al.* 2004; Squires & Quake 2005). However, such insight remains limited to date. This motivates the present study, which seeks to contribute to the present understanding of three-dimensional laminar transport by theoretical and numerical analyses of fundamental transport mechanisms in experimentally realizable three-dimensional model flows.

Unsteady laminar transport is investigated in terms of the three-dimensional advection of passive tracers in the three-dimensional lid-driven cylinder flow introduced by Malyuga *et al.* (2002). The fluid is set in motion through time-periodic forcing by in-plane motion of one endwall via a given forcing protocol. Tracer advection is studied in a Lagrangian framework by examining the topological properties of the coherent structures that form in the three-dimensional web of paths of passive tracers (Malyuga *et al.* 2002; Speetjens, Clercx & van Heijst 2004). Such coherent structures geometrically determine the transport properties of the flow and in-depth knowledge of their formation and topological characteristics, and response to parametric variations is the key to better understanding, and ultimately, systematic manipulation, of three-dimensional mixing. It must be stressed that coherent structures here refer to geometrical entities in the web of Lagrangian tracer paths (e.g. invariant material surfaces). This notion must not be confused with coherent structures in the Eulerian flow field (e.g. vortices).

Theoretical frameworks for three-dimensional Lagrangian transport studies primarily expand on the classical Hamiltonian concept of action-angle variables by (local) representation of coherent structures as invariant surfaces and curves defined by constants of motion, denoted actions in Hamiltonian terminology (see e.g. MacKay 1994; Mezić & Wiggins 1994; Cartwright, Feingold & Piro 1996; Mezić 2001; Gómez & Meiss 2002; Mullowney, Julien & Meiss 2008). A promising recent concept with Hamiltonian foundation and developed specifically for mixing applications is found in the linked twist map (Sturman, Ottino & Wiggins 2006; Meier, Lueptow & Ottino 2007; Sturman *et al.* 2008). Establishment of a comprehensive Hamiltonian-like framework for three-dimensional topological transport studies, and then, in particular, response scenarios to perturbations and routes to chaos, is nonetheless in its infancy. The most important generalization of classical Hamiltonian mechanics to three-dimensional systems is perhaps the three-dimensional counterpart to the well-known Kolmogorov–Arnold–Moser (KAM) theorem describing the fate of invariant tori under weak perturbations (refer e.g. to Cheng & Sun 1990; Mezić & Wiggins 1994; Broer, Huitema & Sevryuk 1996). However, similar universal response scenarios for coherent structures of different topology remain outstanding.

The discussion hereafter concentrates on a fundamental transport phenomenon discovered in previous studies of the above cylinder flow: the merger of coherent structures formed in the non-inertial limit (vanishing Reynolds number Re) into intricate new structures embedded in chaotic regions upon introducing weak fluid

inertia ($Re \lesssim O(0.1)$) (Speetjens, Clercx & van Heijst 2006*a*,*b*). Key to this merger is a mechanism termed resonance-induced merger (RIM) by which coherent structures of the non-inertial limit develop local defects for small $Re > 0$; these defects, in turn, trigger the beforementioned merger with other structures. RIM is important from both a mixing and nonlinear dynamics perspective in that it brings about a qualitative change in three-dimensional transport properties (newly-formed structures have a fundamentally different topology than their non-inertial parents) and opens up an essentially three-dimensional route to global chaos.

Deeper insight into RIM is on two grounds potentially relevant in a wider scope. First, part of the involved coherent structures are spheroidal invariant surfaces, which topologically differ from the classical invariant tori. Second, the non-inertial limit of the present cylinder flow closely relates with configurations considered in literature: (i) generic volume-preserving systems with invariant surfaces (Mezić & Wiggins 1994; Gómez & Meiss 2002; Mullowney *et al.* 2008) and (ii) the continuum representation of tumbled granular flows (Meier *et al.* 2007; Sturman *et al.* 2008). The link with the latter is particularly intimate in that spheroidal invariant surfaces play a central role in both systems. Hence, findings on RIM, and their reconciliation with said systems, may contribute to further development of the beforementioned three-dimensional theoretical framework and application of fundamental insight to realistic transport problems.

Primary objective of the present study is further exploration of the intriguing phenomenon of RIM by addressing the following two issues: (i) establishing the degree of universality of RIM and (ii) paving the way to experimental studies on RIM. To these ends the occurrence and manifestation of RIM is to be examined in a number of cylinder flows that, first, are distinct from one another as well as from that considered in Speetjens *et al.* (2006*a*,*b*) and, second, admit experimental investigations of RIM.

The exposition is organized as follows. Section 2 introduces the physical problem and model flows examined in this study. The theoretical framework for the topological approach towards tracer advection is outlined in § 3. Topological analyses of the model flows in the non-inertial limit are presented in § 4. The response of the several non-inertial topological states to weak fluid inertia is investigated in § 5. Finally, conclusions are drawn in § 6.

2. Problem definition

2.1. *Flow model and tracer kinematics*

Time-periodic flow inside a three-dimensional square cylinder $[r, \theta, z] = [0, R] \times [0, 2\pi] \times [-H/2, H/2]$, with R being the radius and $H = 2R$ being the height, is considered. The fluid is set in motion via time-periodic repetition of a sequence of n piecewise steady translations (forcing steps) of the bottom wall by prescribed forcing protocols. These forcing steps occur at velocity U and are of equal duration $T_{step} = T/n$, with T being the period time of one sequence. A schematic of the configuration is shown in figure 1 (arrows indicate translation directions of the bottom wall) during flow forcing. The forcing protocols will be specified below.

We assume that highly viscous flow conditions such that intermediate unsteady transients during switching between forcing steps are negligible: $T_v/T_{step} = R^2/\nu T_{step} \ll 1$, with $T_v = R^2/\nu$ being the viscous time scale and T_{step} as introduced above. Under this premise the internal flow consists of piecewise steady flows governed by the

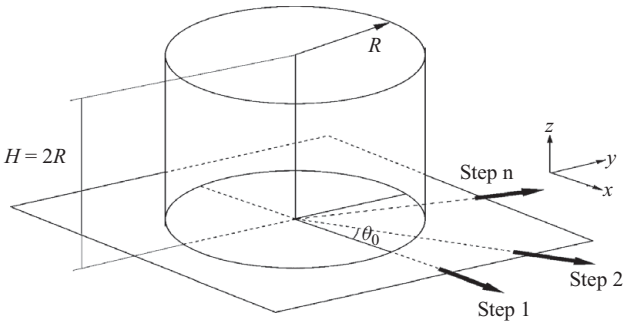

FIGURE 1. Schematic of the three-dimensional cylindrical flow domain and the flow forcing by piecewise steady translations of the bottom wall. R, H and U indicate radius, height and translation velocity, respectively; arrows indicate translation directions of the bottom wall.

non-dimensional steady Navier–Stokes and continuity equations:

$$Re\ \boldsymbol{u}\cdot\nabla\boldsymbol{u} = -\nabla p + \nabla^2\boldsymbol{u}, \quad \nabla\cdot\boldsymbol{u} = 0. \tag{2.1}$$

The motion of passive tracers in this flow is governed by the kinematic equation:

$$\frac{\mathrm{d}\boldsymbol{x}}{\mathrm{d}t} = \boldsymbol{u}, \quad \boldsymbol{x}(0) = \boldsymbol{x}_0, \tag{2.2}$$

which describes the evolution of the positions $\boldsymbol{x}(t)$ of tracers released at $\boldsymbol{x}_0$. The general solution to (2.2) reads $\boldsymbol{x}(t) = \boldsymbol{\Phi}_t(\boldsymbol{x}_0)$ and uniquely determines the current position $\boldsymbol{x}$ for a given initial tracer position $\boldsymbol{x}_0$. The corresponding discrete mapping is defined by $\boldsymbol{x}_{k+1} = \boldsymbol{\Phi}_T(\boldsymbol{x}_k)$, where $\boldsymbol{x}_k$ is the tracer position after k periods of the time-periodic forcing protocol. The remainder of the study concerns discrete mappings $\boldsymbol{\Phi}_T$ only, the subscript T of which are dropped for brevity. The corresponding tracer dynamics will be investigated in terms of Poincaré sections; these are the subsequent tracer positions after each period as if illuminated by a stroboscope in phase with the flow forcing (Ottino 1989). The Poincaré sections of tracers released at strategic locations in the domain enable visualization of the flow topology. The composition of this flow topology is determined by several features, which will be discussed in § 3.

2.2. *Forcing protocols*

Protocol-$\mathscr{A}$' is a two-step forcing protocol; the first step is in the positive x-direction; the second step is under an angle $0 \leqslant \theta_0 \leqslant \pi$ with respect to the x-axis:

$$\boldsymbol{\Phi}^{\mathscr{A}'} = \begin{cases} \boldsymbol{\Phi}_1 : U \text{ in } \theta = 0 \text{ direction} & 0 \leqslant t < \dfrac{T}{2}, \\ \boldsymbol{\Phi}_2 : U \text{ in } \theta = \theta_0 \text{ direction with respect to } x\text{-axis} & \dfrac{T}{2} \leqslant t < T. \end{cases} \tag{2.3}$$

The general family of two-step forcing protocols has been termed Protocol-$\mathscr{A}$', this is a generalization of Protocol-$\mathscr{A}$' considered in Speetjens *et al.* (2004) ($\theta_0 = \pi/2$). Protocol-$\mathscr{A}$' is schematically shown in figure 2(a). The arrows indicate direction of motion of the bottom wall during the forcing steps.

The second protocol is a three-step forcing protocol with the bottom wall describing a closed path along an equilateral triangle ($\theta_0 = 2\pi/3$) following figure 2(b). It is

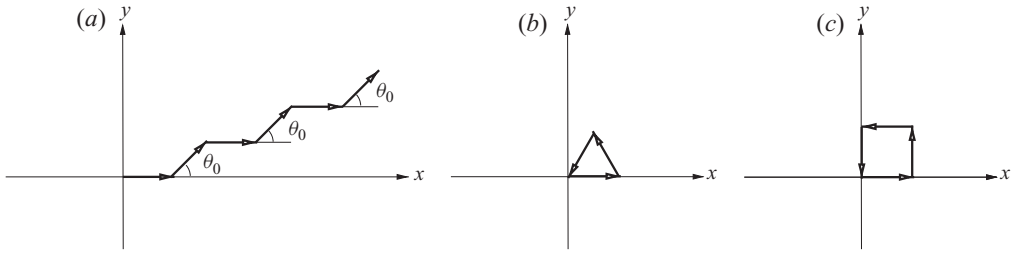

FIGURE 2. Time-periodic forcing protocols. (*a*) Two-step open forcing according to Protocol-$\mathscr{A}$'; (*b*) three-step closed forcing according to Protocol-$\mathscr{T}$; (*c*) four-step closed forcing according to Protocol-$\mathscr{S}$. Arrows indicate path followed by bottom wall.

denoted Protocol-$\mathscr{T}$ and defined according to:

$$\boldsymbol{\Phi}^{\mathscr{T}} = \begin{cases} \boldsymbol{\Phi}_1 : U \text{ in } \theta = 0 \text{ direction} & 0 \leqslant t < \dfrac{T}{3}, \\ \boldsymbol{\Phi}_2 : U \text{ in } \theta = 2\pi/3 \text{ direction} & \dfrac{T}{3} \leqslant t < \dfrac{2T}{3}, \\ \boldsymbol{\Phi}_3 : U \text{ in } \theta = 4\pi/3 \text{ direction} & \dfrac{2T}{3} \leqslant t < T. \end{cases} \tag{2.4}$$

The third protocol is a four-step forcing protocol with the bottom wall describing a closed path along a square ($\theta_0 = \pi/2$) following figure 2(*c*). It is denoted Protocol-$\mathscr{S}$ and defined as:

$$\boldsymbol{\Phi}^{\mathscr{S}} = \begin{cases} \boldsymbol{\Phi}_1 : U \text{ in } \theta = 0 \text{ direction} & 0 \leqslant t < \dfrac{T}{4}, \\ \boldsymbol{\Phi}_2 : U \text{ in } \theta = \pi/2 \text{ direction} & \dfrac{T}{4} \leqslant t < \dfrac{T}{2}, \\ \boldsymbol{\Phi}_3 : U \text{ in } \theta = \pi \text{ direction} & \dfrac{T}{2} \leqslant t < \dfrac{3T}{4}, \\ \boldsymbol{\Phi}_4 : U \text{ in } \theta = 3\pi/2 \text{ direction} & \dfrac{3T}{4} \leqslant t < T. \end{cases} \tag{2.5}$$

Protocol-$\mathscr{A}$' is an open protocol in the sense that the wall follows an open path. Repetition for many periods thus, in practice, requires an infinitely large moving wall. This renders Protocol-$\mathscr{A}$' unsuitable for long-term laboratory experiments. Protocols-$\mathscr{T}$ and $\mathscr{S}$, on the other hand, are both closed protocols that can be repeated indefinitely with a finite-size wall. This makes them well suited for laboratory experiments.

The piecewise steady nature of the flow restricts time-dependence to the instantaneous change of direction after each forcing step. This implies that, instead of the period time T, the non-dimensional wall displacement during each forcing step, given by

$$D = \frac{UT}{nR} \tag{2.6}$$

is the relevant kinematic parameter. Thus, each forcing protocol is controlled by two system parameters: Re and D.

Numerical resolution of the flow model (2.1) is performed by means of the spectral scheme proposed in Speetjens & Clercx (2005). This algorithm yields highly accurate solutions that admit satisfaction of the incompressibility constraint $\nabla \cdot \boldsymbol{u} = 0$ up to near-machine precision. Performance analysis advanced highly accurate conservation

of this constraint as an essential prerequisite for reliable numerical studies on tracer advection in volume-preserving systems that conventional schemes tend to fall short of Speetjens & Clercx (2005). Numerical integration of the kinematic equation (2.2) employs an explicit third-order Taylor–Galerkin scheme and an interpolation scheme for the velocity field based upon its spectral expansion. Important to note is that the spectral scheme on numerical grounds imposes $U_* = U(r^2-1)^2$ instead of the constant translation velocity U for the bottom wall. This is irrelevant to the present study, however. Key topological properties of the non-inertial baseline flow are identical for both boundary conditions: (i) closed streamlines self-symmetric about $x=0$ and symmetrically arranged about $y=0$ and (ii) presence of axisymmetric spheroidal invariant surfaces. This, in consequence, implies that the non-inertial time-periodic flows have the same symmetry properties and the same kind of invariant surfaces, and therefore are topologically equivalent, for both boundary conditions. This particular topological make-up plays a central role in the present study. (The relevance of such features is discussed in more detail below.) Hence, results discussed hereafter are fully representative of the physical situation. This modification manifests itself only in quantitative sense in that physical topological features may differ slightly in shape and physical Reynolds numbers corresponding with U are an estimated factor two lower compared to their counterparts corresponding with boundary condition U_* (Speetjens 2001).

3. Flow topology: relevant features

The flow topology in the Poincaré section is organized into coherent structures. Extensive discussions on this topic may be found in e.g. Malyuga *et al.* (2002) and Speetjens *et al.* (2004). The coherent structures and organizing properties relevant in the current scope are periodic lines, specific symmetries and invariant surfaces associated with constants of motion. These topological features are briefly discussed below.

3.1. *Periodic lines*

Periodic points of order p (or period-p points) of a time-periodic map are material points that will return to their initial positions after p periods: $\boldsymbol{X} = \boldsymbol{\Phi}^p(\boldsymbol{X})$. The local behaviour at such period-p points is determined by

$$\mathrm{d}\boldsymbol{x}_{n+1} = \boldsymbol{F}\cdot\mathrm{d}\boldsymbol{x}_n, \quad \boldsymbol{F} = \nabla\boldsymbol{\Phi}^p|_{\boldsymbol{X}} = \sum_{i=1}^{3}\lambda_i\boldsymbol{n}_i\boldsymbol{n}_i, \tag{3.1}$$

with $\mathrm{d}\boldsymbol{x}$ being the local frame of reference, $\boldsymbol{F}$ being the deformation tensor representing the locally linearized mapping $\boldsymbol{\Phi}$ and $\{\lambda_i, \boldsymbol{n}_i\}$ being its spectral decomposition (Malyuga *et al.* 2002). The eigenvalue spectrum $\boldsymbol{\Lambda} = \{\lambda_1, \lambda_2, \lambda_3\}$ determines the local dynamics and thus the type of periodic point, where solenoidality of the flow field $\boldsymbol{u}$ implies $\lambda_1\lambda_2\lambda_3 = 1$.

The complex dynamics of chaotic systems is intimately related to the emergence of (in particular, lower-order) periodic points in the flow (Ottino 1989; Ott 1993). In three-dimensional space, periodic points may either appear isolated or merge into periodic lines. In the present context, only periodic lines are relevant and, consequently, the recapitulation of topological features below pertains only to these entities.

Periodic lines are in essence the three-dimensional counterparts of periodic points in two-dimensional systems in that they induce effectively two-dimensional tracer dynamics in the local plane perpendicular to their tangent (here, each constituent

point is periodic and not the whole periodic line). This tangent coincides with one of the eigenvectors of $\boldsymbol{F}$, say $\boldsymbol{n}_1$, that has a corresponding eigenvalue $\lambda_1 = 1$, signifying absence of motion in $\boldsymbol{n}_1$-direction. Eigenvectors $\boldsymbol{n}_{2,3}$ are normal to $\boldsymbol{n}_1$ and span the beforementioned perpendicular plane; the associated eigenvalues dictate the dynamics within this plane and are governed by

$$\lambda_{2,3} = \frac{J-1}{2} \pm \sqrt{\mathscr{D}}, \quad \mathscr{D} = \frac{(J-1)^2}{4} - 1, \tag{3.2}$$

with $J = \mathrm{trace}(\boldsymbol{F})$ and $\mathscr{D}$ being the discriminant (Malyuga *et al.* 2002). (Cases with $\lambda_1 \neq 1$ correspond to isolated periodic points. However, in the present context, only periodic lines (consisting of periodic points with $\lambda_1 = 1$) are relevant.) Two non-degenerate types of periodic points in two-dimensional systems and, consequently, two non-degenerate types of (segments of) periodic lines can be distinguished (Malyuga *et al.* 2002):

(i) Elliptic type ($\mathscr{D} < 0$): $\boldsymbol{\Lambda} = \{1, e^{\mathrm{i}\phi}, e^{-\mathrm{i}\phi}\}$: Elliptic points on periodic lines form the centres of elliptic islands within the local perpendicular plane that consist of concentric closed orbits along which tracers undergo periodwise rotation at an angle ϕ. In three-dimensional, these islands merge into elliptic tubes centred on elliptic (segments of) periodic lines. Such tubes entrap and circulate tracers and thus form barriers to global tracer transport. This, consequently, leads to efficient mixing.

(ii) Hyperbolic type ($\mathscr{D} > 0$): $\boldsymbol{\Lambda} = \{1, \lambda, 1/\lambda\}$: Hyperbolic points on periodic lines are the time-periodic equivalent of saddle points in two-dimensional systems; the associated stable and unstable manifolds delineate the principal transport directions within the local perpendicular plane. Material is elongated along the unstable manifold by a stretching rate $\lambda > 1$ and is compressed along the stable manifold by a compression rate $1/\lambda < 1$. In three-dimensional, the planar manifolds merge into two-dimensional manifolds (i.e. surfaces) emanating from hyperbolic (segments of) periodic lines. Transverse manifold intersection leads to exponential stretching of material elements and, inherently, chaotic tracer advection.

Elliptic and hyperbolic segments on periodic lines are connected by parabolic points ($\mathscr{D} = 0$ and $\boldsymbol{\Lambda} = \{1, 1, 1\}$). These are degenerate points in that, contrary to elliptic and hyperbolic points, in the Poincaré section net fluid motion ceases in their proximity. This particular behaviour near parabolic points will have fundamental ramifications for the flow topology under weakly inertial conditions. This will be addressed in § 5. Note that segmented periodic lines are a generalization of the single-type periodic lines (alternatively termed normally hyperbolic/elliptic invariant curves) discussed in Mezić & Wiggins (1994), Meier *et al.* (2007) and Sturman *et al.* (2008).

3.2. *Symmetries*

Symmetries are essential properties in that they organize the flow topology – and thus affect the tracer dynamics – and facilitate identification of coherent structures (Franjione, Leong & Ottino 1989; Ottino, Jana & Chakravarthy 1994; Meleshko & Peters 1996). Two types of symmetries are relevant in the present context: (i) time-reversal reflectional symmetries and (ii) ordinary non-reflectional symmetries. The characteristics of these symmetries and their role in the flow topology and tracer dynamics are elaborated below.

Periodic lines are intimately related to the so-called time-reversal reflectional symmetries of the mapping $\boldsymbol{\Phi}$ (Speetjens *et al.* 2004). These are symmetries of the form

$$\boldsymbol{\Phi} = S\boldsymbol{\Phi}^{-1}S, \tag{3.3}$$

where $S = S^{-1}$ effectuates reflection about the associated symmetry plane I_S, defined as $I_S = S(I_S)$. (Note that generic symmetry relations between operators $\boldsymbol{A}$ and $\boldsymbol{B}$ are of the form $\boldsymbol{A} = S\boldsymbol{B}S^{-1}$. For reflectional symmetries this relation becomes $\boldsymbol{A} = S\boldsymbol{B}S$ due to $S = S^{-1}$.) Important in the present context is that time-reversal reflectional symmetries of the form (3.3) imply periodic lines in the symmetry plane I_S. This enables systematic and efficient isolation of periodic lines. Roughly, the procedure can be explained as follows. A material surface is released on the symmetry plane I_S and tracked for one period. The intersection of the original and tracked surfaces corresponds with a period-1 line. Similarly, higher-order periodic lines can be found in I_S. Note that, in principle, further periodic lines may exist outside the symmetry plane I_S. However, the present study concentrates specifically on tracer dynamics related with the period-1 line within I_S.

Time-reversal reflectional symmetries in the present mappings of the form

$$\boldsymbol{\Phi} = \boldsymbol{\Phi}_n \boldsymbol{\Phi}_{n-1} \cdots \boldsymbol{\Phi}_1, \tag{3.4}$$

derive from symmetries of the individual forcing steps. Two types are relevant in this respect: time-reversal and ordinary reflectional symmetries within and between steps. This leads to four kinds of reflectional symmetry relations for the forcing steps, namely

$$\boldsymbol{\Phi}_i = S\boldsymbol{\Phi}_i S \quad \boldsymbol{\Phi}_i = S{\boldsymbol{\Phi}_i}^{-1} S \quad \boldsymbol{\Phi}_i = S\boldsymbol{\Phi}_j S \quad \boldsymbol{\Phi}_i = S{\boldsymbol{\Phi}_j}^{-1} S, \tag{3.5}$$

with subscripts i and j indicating different steps. These symmetry relations can, for given forcing protocols, be identified via methods discussed in e.g. Malyuga *et al.* (2002).

The second type of symmetries relevant in the present context are ordinary symmetries

$$\boldsymbol{\Phi} = S\boldsymbol{\Phi}S^{-1}, \tag{3.6}$$

which, in contrast with the generic connection between time-reversal reflectional symmetries and periodic lines, affect the flow topology and tracer dynamics in very case-specific ways (Meleshko & Peters 1996; Malyuga *et al.* 2002). Here, such symmetries play a pivotal role in the response of the flow topology to inertial perturbations.

3.3. *Invariant surfaces*

Invariant surfaces are material surfaces within which tracers remain trapped indefinitely. Such surfaces may emanate from either particular symmetries or constants of motion (Bajer 1994). Here, the latter case is of relevance.

Constants of motion are quantities G that are preserved by fluid elements during their excursion in the flow domain. In the current scope of piecewise steady flows, only constants of motion without explicit time-dependence are considered: $G = G(\boldsymbol{x})$. Preservation by fluid elements means they satisfy

$$\frac{\mathrm{d}G}{\mathrm{d}t} = \boldsymbol{u} \cdot \nabla G = 0, \quad G(\boldsymbol{x}) = G(\boldsymbol{x}_0), \tag{3.7}$$

revealing that a tracer released at $\boldsymbol{x}_0$ remains trapped within the material surface defined by the surface $G(\boldsymbol{x}_0)$. Thus, in three-dimensional flows, constants of motions parameterize families of iso-surfaces $G = \text{constant}$, within which tracers perform an effectively two-dimensional motion. Absence of explicit time-dependence in G implies that these invariant surfaces remain fixed in space at any time.

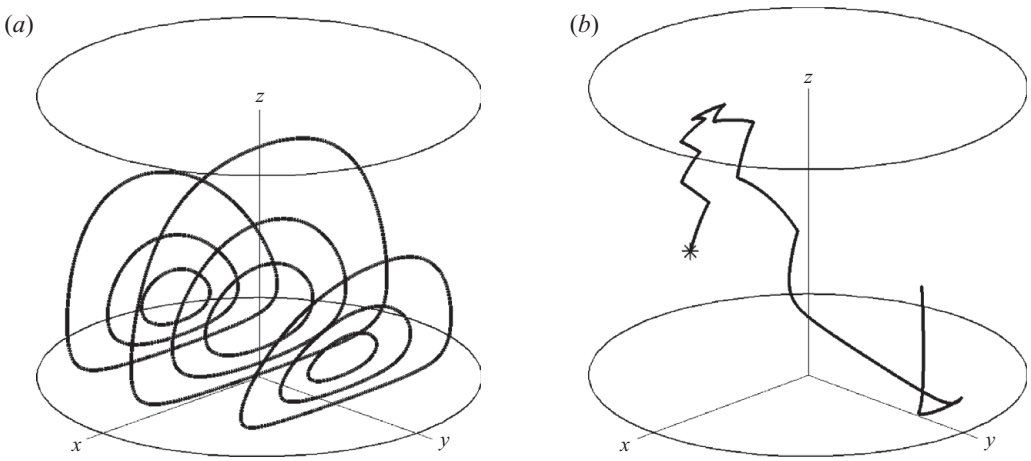

FIGURE 3. Typical tracer paths: (*a*) closed streamlines of the base flow (steady translation bottom wall in x-direction) and (*b*) open trajectory in Protocol-$\mathscr{A}$' (star indicates initial position).

4. Flow topology: non-inertial limit ($Re = 0$)

4.1. *Introduction*

The non-inertial limit ($Re = 0$) serves as the baseline flow for examination of the inertial perturbations of the flow. The piecewise steady flows are in the non-inertial limit governed by the Stokes and continuity equations

$$-\nabla p + \nabla^2 \boldsymbol{u} = 0 \quad \nabla \cdot \boldsymbol{u} = 0, \tag{4.1}$$

coinciding with (2.1) for $Re = 0$ and are rotations of the base flow set up by steady translation of the bottom wall in x-direction. Figure 3(*a*) gives this base flow, consisting mainly of one large vortex with closed streamlines that are self-symmetric about the plane $x = 0$ and form symmetric pairs about the plane $y = 0$ (Shankar 1997).

The tracer paths of the time-periodic flows consist of segments of the streamlines of the consecutive forcing steps. This is demonstrated in figure 3(*b*), where a typical tracer path is given for the two-step forcing protocol-$\mathscr{A}$'. These tracer paths, in contrast with the closed streamlines of the steady baseline flow in figure 3(*a*), are open and thereby admit greater freedom of motion. This openness of tracer paths is an essential (yet not sufficient) ingredient for chaotic advection – and thus efficient mixing.

4.2. *Symmetry analysis*

Time-reversal reflectional symmetries (3.3), if existent, enable efficient and systematic isolation of period-1 lines in the forcing protocols; such lines coincide with the associated symmetry plane I_S (§ 3). Furthermore, ordinary symmetries (3.6) may provide further insight into the case-specific dynamics of the forcing protocols (Malyuga *et al.* 2002). Such global symmetries can be derived from symmetry relations of the form (3.5) between the forcing steps. The symmetry relations for the forcing protocols considered here are derived below.

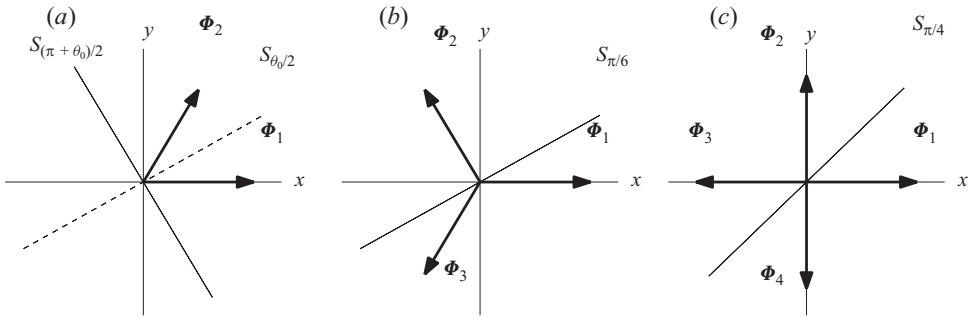

FIGURE 4. The symmetry planes of the different forcing protocols. (*a*) Protocol-$\mathscr{A}$': $\theta = (\pi + \theta_0)/2$, (*b*) Protocol-$\mathscr{T}$: $\theta = \pi/6$ and (*c*) Protocol-$\mathscr{S}$: $\theta = \pi/4$.

The symmetry properties of the forcing steps of Protocol-$\mathscr{A}$' can be determined in the same way as discussed in Speetjens *et al.* (2004). This yields

$$\boldsymbol{\Phi}_1 = S_{(\pi+\theta_0)/2}\boldsymbol{\Phi}_2^{-1}S_{(\pi+\theta_0)/2}, \quad \boldsymbol{\Phi}_2 = S_{(\pi+\theta_0)/2}\boldsymbol{\Phi}_1^{-1}S_{(\pi+\theta_0)/2},$$
$$\boldsymbol{\Phi}_1 = S_{\theta_0/2}\boldsymbol{\Phi}_2 S_{\theta_0/2}, \quad \boldsymbol{\Phi}_2 = S_{\theta_0/2}\boldsymbol{\Phi}_1 S_{\theta_0/2},$$

as particular symmetry relations relevant here, with $S_{(\pi+\theta_0)/2}$ being a reflection about the plane $\theta = (\pi + \theta_0)/2$ (figure 4*a*) and, likewise, $S_{\theta_0/2}$ being a reflection about the plane $\theta = \theta_0/2$. Substitution of the time-reversal symmetries into (3.4) ($n = 2$) leads to

$$\begin{aligned}\boldsymbol{\Phi} &= S_{(\pi+\theta_0)/2}\boldsymbol{\Phi}_1^{-1}S_{(\pi+\theta_0)/2}S_{(\pi+\theta_0)/2}\boldsymbol{\Phi}_2^{-1}S_{(\pi+\theta_0)/2}\\ &= S_{(\pi+\theta_0)/2}\boldsymbol{\Phi}_1^{-1}\boldsymbol{\Phi}_2^{-1}S_{(\pi+\theta_0)/2}\\ &= S_{(\pi+\theta_0)/2}\boldsymbol{\Phi}^{-1}S_{(\pi+\theta_0)/2},\end{aligned} \tag{4.2}$$

as time-reversal reflectional symmetry for Protocol-$\mathscr{A}$' about plane $\theta = (\pi + \theta_0)/2$. The existence of this symmetry means that this forcing protocol always possesses a period-1 line, located within its symmetry plane. Similarly, an ordinary symmetry is identified via

$$\boldsymbol{\Phi} = S_{\theta_0/2}\boldsymbol{\Phi}_1 S_{\theta_0/2}S_{\theta_0/2}\boldsymbol{\Phi}_2 S_{\theta_0/2} = S_{\theta_0/2}\boldsymbol{\Phi}_1\boldsymbol{\Phi}_2 S_{\theta_0/2} = \widetilde{S}\boldsymbol{\Phi}\widetilde{S}^{-1}, \tag{4.3}$$

with $\widetilde{S} = S_{\theta_0/2}\boldsymbol{\Phi}_1$. This symmetry has essential consequences for the response of the flow topology to inertial perturbations (§ 5).

The flows due to the closed forcing protocols are structurally similar to the reoriented duct flow considered in Speetjens, Metcalfe & Rudman (2006*c*) in that they consist of a sequence of reorientations of the base flow that together describe a closed loop. Therefore, the symmetry properties are equivalent. The symmetry properties of the forcing steps read

$$\left.\begin{aligned}\boldsymbol{\Phi}_1 &= S_{(\pi-\theta_0)/2}\boldsymbol{\Phi}_n^{-1}S_{(\pi-\theta_0)/2},\\ \boldsymbol{\Phi}_2 &= S_{(\pi-\theta_0)/2}\boldsymbol{\Phi}_{n-1}^{-1}S_{(\pi-\theta_0)/2}, \ldots,\\ \boldsymbol{\Phi}_n &= S_{(\pi-\theta_0)/2}\boldsymbol{\Phi}_1^{-1}S_{(\pi-\theta_0)/2},\end{aligned}\right\} \tag{4.4}$$

with $S_{(\pi-\theta_0)/2}$ being a reflection about the plane $\theta = (\pi - \theta_0)/2$. Substitution into (3.4) gives

$$\begin{aligned}\boldsymbol{\Phi} &= S_{(\pi-\theta_0)/2}\boldsymbol{\Phi}_1^{-1}S_{(\pi-\theta_0)/2}S_{(\pi-\theta_0)/2}\boldsymbol{\Phi}_2^{-1}S_{(\pi-\theta_0)/2}\cdots S_{(\pi-\theta_0)/2}\boldsymbol{\Phi}_n^{-1}S_{(\pi-\theta_0)/2}\\ &= S_{(\pi-\theta_0)/2}\boldsymbol{\Phi}^{-1}S_{(\pi-\theta_0)/2},\end{aligned}$$

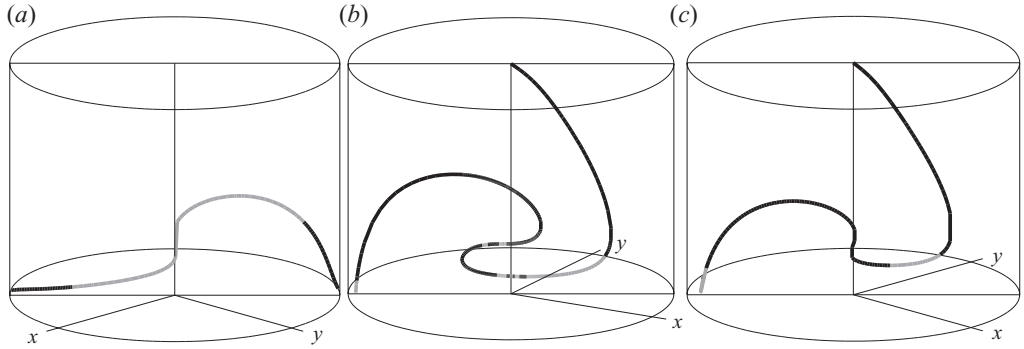

FIGURE 5. Typical period-1 lines (curves) inside their symmetry planes (rectangular outline). (*a*) Protocol-$\mathscr{A}$' for $\theta_0 = \pi/2$ and $D = 5$, (*b*) Protocol-$\mathscr{T}$ for $D = 14$ and (*c*) Protocol-$\mathscr{S}$ for $D = 10$. Dark and bright regions indicate elliptic and hyperbolic segments on the period-1 lines, respectively. Views are into the symmetry planes.

as time-reversal reflectional symmetry about plane $\theta = (\pi - \theta_0)/2$. For the particular forcings according to Protocol-$\mathscr{T}$ ($\theta_0 = 2\pi/3$) and Protocol-$\mathscr{S}$ ($\theta_0 = \pi/2$), this implies symmetry planes $\theta = \pi/6$ (figure 4*b*) and $\theta = \pi/4$ (figure 4*c*), respectively.

Thus, closed protocols, similar to the open Protocol-$\mathscr{A}$', also always possess a period-1 line. Essential difference with the latter is that an additional symmetry as (4.3) is absent here. This causes important differences between the response of Protocol-$\mathscr{T}$ and $\mathscr{S}$ to inertial perturbations compared to that of Protocol-$\mathscr{A}$', as will be shown in § 5.

4.3. *Period-1 lines*

The above symmetry analysis revealed that the present forcing protocols all possess time-reversal reflectional symmetries. This implies that period-1 lines sit within the corresponding symmetry planes (figure 4) and can therefore be isolated by the procedure outlined in § 3.

Figure 5(*a*) shows the period-1 line for Protocol-$\mathscr{A}$' for $\theta_0 = \pi/2$ and $D = 5$ (curve) inside the symmetry plane $\theta = 3\pi/4$ (rectangular outline). The dark and bright segments of the period-1 line indicate elliptic and hyperbolic segments, respectively. Note that the period-1 line is invariant under the ordinary symmetry $\widetilde{S}$ according to (4.3). Figures 5(*b*) and (*c*) give the period-1 lines for Protocol-$\mathscr{T}$ ($D = 14$) and Protocol-$\mathscr{S}$ ($D = 10$), respectively, in the symmetry planes $\theta = \pi/6$ and $\theta = \pi/4$. Both period-1 lines are significantly more convoluted than those of Protocol-$\mathscr{A}$' and, moreover, exhibit stronger segmentation into hyperbolic and elliptic regions. These effects are direct consequences of the greater complexity of the flow field compared to Protocol-$\mathscr{A}$'. Furthermore, the segmentation of periodic lines is essential to the response to inertial perturbations investigated in § 5.

Variation of the displacement D brings about great changes in both shape and segmentation of the period-1 lines. This is demonstrated for Protocol-$\mathscr{T}$ in figure 6, where the progression of the period-1 line in the symmetry plane $\theta = \pi/6$ is shown for increasing D, with elliptic and hyperbolic segments indicated as before. By increasing D, both the shape of the period-1 line and the extent of hyperbolic and elliptic segments change dramatically. The shape becomes progressively convoluted with growing D; the segmentation, on the other hand, exhibits a strongly nonlinear dependence upon D. The progression of shape and segmentation of the period-1 line for Protocol-$\mathscr{S}$ is very similar to that shown in figure 6.

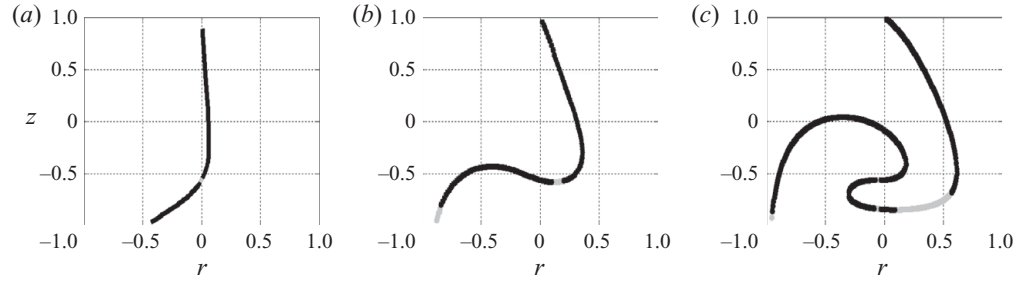

FIGURE 6. Period-1 line of Protocol-$\mathscr{T}$ shown within the symmetry plane $\theta = \pi/6$ as a function of the displacement D. (a) $D = 1$, (b) $D = 6$ and (c) $D = 14$. Dark and bright regions indicate elliptic and hyperbolic segments on the period-1 line, respectively.

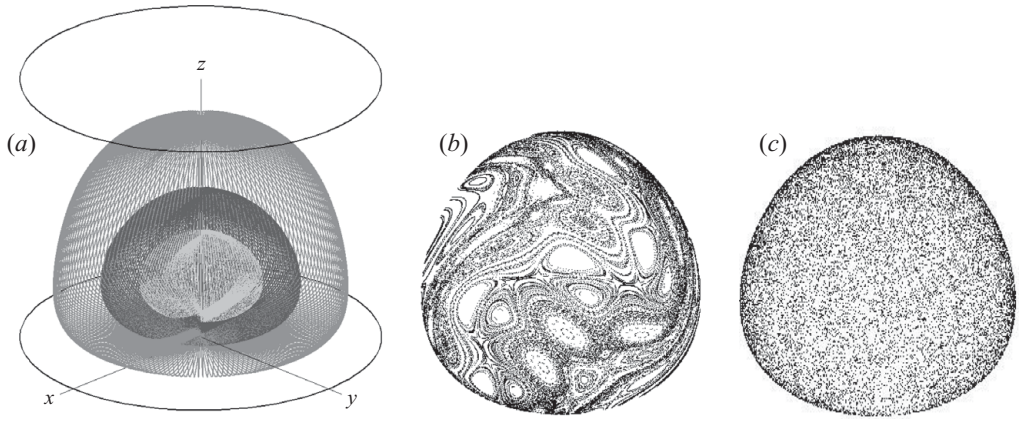

FIGURE 7. Axisymmetric invariant surfaces and intra-surface dynamics. (a) Typical surfaces and their concentric arrangement, (b) typical intra-surface dynamics containing elliptic islands and chaotic regions and (c) fully chaotic intra-surface dynamics.

4.4. *Invariant surfaces and intra-surface dynamics*

The flows which are studied here have one constant of motion according to (3.7) with axisymmetric invariant surfaces that are topologically equivalent to spheres and concentrically arranged according to figure 7(a) (Malyuga *et al.* 2002). These invariant surfaces imply effectively two-dimensional tracer motion (§ 3). Moreover, the underlying constant of motion in combination with continuity implies that non-degenerate periodic points dictating the intra-surface dynamics must be of the elliptic or hyperbolic type (Gómez & Meiss 2002). Here, these periodic points correspond with the intersection of the elliptic/hyperbolic (segments of) periodic lines and the invariant surfaces. This has the important implication that the intra-surface motion is essentially equivalent to that of two-dimensional time-periodic Hamiltonian systems. This is demonstrated in figure 7 by the Poincaré sections of tracers released within one invariant surface, revealing characteristic Hamiltonian dynamics. Figure 7(b) gives an example with multiple chains of elliptic islands embedded within chaotic seas; figure 7(c) with fully chaotic tracer motion. The Hamiltonian nature of the intra-surface dynamics is investigated further below.

The intra-surface dynamics depends on two parameters: the bottom-wall displacement D and the radius r_s of the invariant surface (defined as the horizontal distance from the invariant surfaces to the stagnation point on the cylinder axis

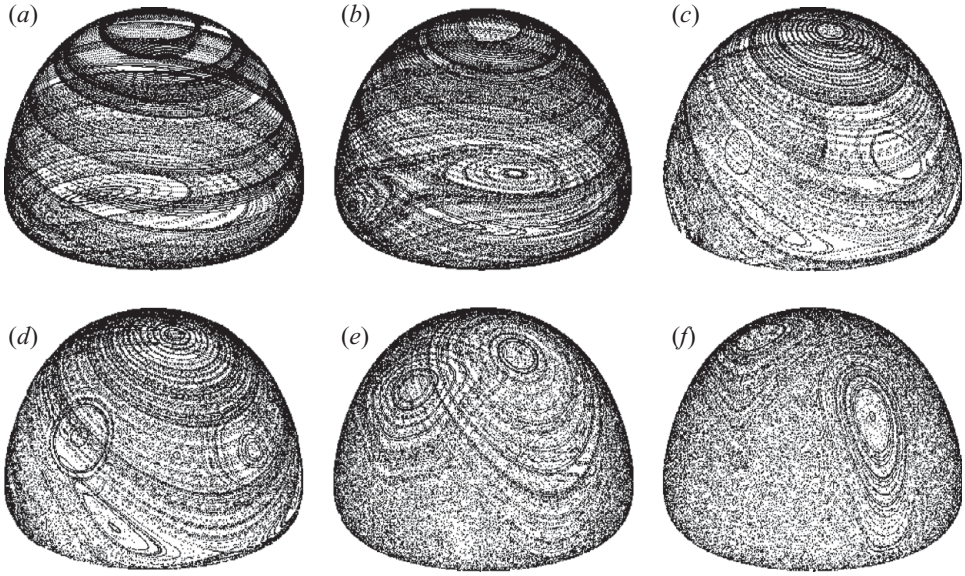

FIGURE 8. Evolution of the intra-surface dynamics with increasing displacement D demonstrated for Protocol-$\mathscr{T}$ in a given invariant surface. (*a*) $D=2$, (*b*) $D=3$, (*c*) $D=5$, (*d*) $D=6$, (*e*) $D=10$ and (*f*) $D=17$.

that forms their common centre). Variations in these parameters result in changes in dynamics similar to those found upon perturbation of two-dimensional Hamiltonian systems. The progressions in intra-surface dynamics with variation of the above parameters – inextricably linked with the segmentation of periodic lines – are of particular importance for the response of the flow topology to inertial perturbations.

First, the effect of variation of the displacement D is considered. This is demonstrated in figure 8 for one invariant surface of Protocol-$\mathscr{T}$. For very short displacement, tracers describe closed and nearly parallel orbits around the cylinder axis (not shown), resulting in the formation of two adjacent period-1 elliptic islands, centred on elliptic points near the two intersections of the surface with the cylinder axis, covering the entire surface (figure 8*a*). This state corresponds dynamically with an integrable Hamiltonian system. This is a state for which all trajectories are fully known and predictable. States consisting entirely of elliptic islands are integrable; states exhibiting (local) chaotic dynamics are non-integrable (Ott 1993). This is important to note that the boundary between both islands cannot be determined; this may, in principle, be any closed orbit between both centres. Increasing the displacement causes breakup of the bottom period-1 island into two period-2 islands separated by a narrow chaotic band (figure 8*b*). (This is consistent with period-doubling bifurcations known from Hamiltonian mechanics.) Growing displacement causes expansion of the two period-2 islands, followed by their breakup into further islands and the formation of a surrounding chaotic sea (figures 8*c* and 8*d*). The top island, meanwhile, remains intact and only diminishes in size somewhat while gradually wandering downhill along the facing side of the invariant surface. Further increasing D causes expansion of the chaotic sea at the expense of the islands originating from the bottom island, save one surviving island on the rear side of the invariant surface, and further diminution and downward migration of the (original) top island on the facing side (figures 8*e* and 8*f*). This evolution with increasing D is essentially similar to that of a two-dimensional

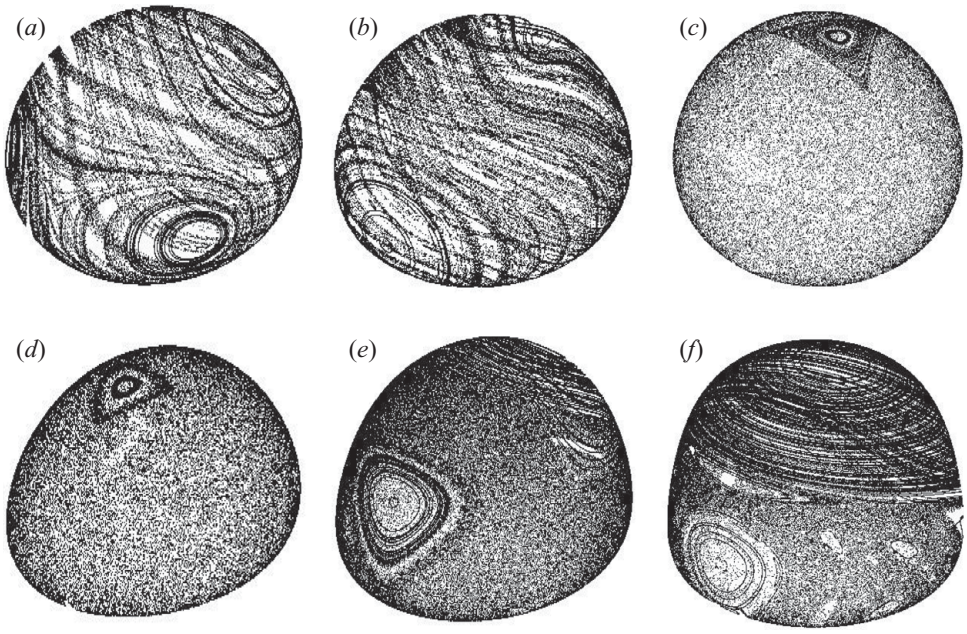

FIGURE 9. Evolution of the intra-surface dynamics with increasing radius r_s of the invariant surface demonstrated for Protocol-$\mathscr{T}$ with given displacement $D = 14$. (*a*) $r_s = 0.125$; (*b*) $r_s = 0.25$; (*c*) $r_s = 0.325$; (*d*) $r_s = 0.5$; (*e*) $r_s = 0.75$; (*f*) $r_s = 0.825$. Note that shown surfaces are not to scale; they increase in size from panels (*a*) to (*f*) in the actual configuration.

Hamiltonian system upon progressive departure from its integrable state (Ott 1993). Moreover, it generally depends nonlinearly on the perturbation parameter (here D) in that stronger perturbation must not necessarily result in more chaotic dynamics; existing islands, after diminution, may again grow in size or new islands may form.

The evolution of the intra-surface dynamics as a function of the radius of the invariant surface is demonstrated in figure 9 for Protocol-$\mathscr{T}$ at the given displacement $D = 14$. This evolution has basically the same Hamiltonian characteristics as that shown for variation of D in figure 8: nonlinear progression of the flow topology with monotonic variation of the perturbation parameter r_s. (Radius r_s parameterizes the intra-surface dynamics upon progressing through the invariant surfaces from their common centre towards the cylinder wall. It is not a perturbation parameter in the strict sense though, since it cannot be controlled externally.) However, essential difference with the above is that here the progression takes place between two (protocol-independent) integrable states: $r_s = 0$ (stagnation point) and $r_s = R$ (no-slip boundary). Figure 9(*a*) shows the invariant surface at $r_s = 0.125$, closest to the integrable state $r_s = 0$, which is covered by three elliptic islands that are separated by narrow chaotic bands (not indicated). Increasing the radius to $r_s = 0.25$ causes coalescence of the two islands on the bottom side of the surface, resulting in a state comprising two elliptic islands, occupying bottom and top sides of the surface (figure 9*b*). By increasing the radius further, the island on the bottom side entirely disappears in favour of a chaotic sea, while the top island remains intact yet decreases significantly in size (figure 9*c*). Further progression of r_s reveals migration of the top island from the facing side (figure 9*c*) towards the rear side (figures 9*d* and 9*e*) of the invariant surface while growing in size; this migration is accompanied by the

emergence of a new island on the top of the surface (figure 9*e*). This island rapidly increases in size and covers the top half of the invariant surface while further smaller islands appear in the chaotic sea (figure 9*f*). This reflects the fact that the tracer dynamics become more regular upon approaching the outer integrable state (i.e. no-slip boundary). This sets in from top down due to the fact that the flow forcing occurs via the bottom wall.

The progressions for Protocol-$\mathscr{A}$' and Protocol-$\mathscr{S}$ are in essence the same in that they qualitatively follow the scenarios demonstrated above for Protocol-$\mathscr{T}$. Differences manifest themselves predominantly in the composition of the flow topologies. More elaborate forcing protocols, for instance, tend to result in more complex topologies. A further difference is that for the open Protocol-$\mathscr{A}$' the chaotic seas grow substantially larger with increasing r_s – and typically cover entire invariant surfaces – and the dynamics becoming more regular upon approaching the no-slip boundary sets in for higher r_s than in the closed Protocols-$\mathscr{T}$ and $\mathscr{S}$. The behaviour found for Protocol-$\mathscr{A}$' in Speetjens *et al.* (2006*a*) and simulations of other open forcings (not shown) strongly suggest this to be a generic difference between open and closed forcing protocols. Thus the closed forcing protocols tend to be dynamically more constrained than their open counterparts in the sense that global chaos is less likely to occur and, instead, arrangements of islands remain present. This has important consequences for the response to inertial perturbations. This will be discussed in § 5.

Better understanding of the response to perturbations is for two reasons of potential importance in a broader context. First, part of the involved coherent structures are spheroidal invariant surfaces, which topologically differ from the classical invariant tori. Second, the non-inertial limit of the present cylinder flow closely relates with configurations considered in literature, viz. with generic volume-preserving systems accommodating invariant surfaces (Mezić & Wiggins 1994; Gómez & Meiss 2002) and with the continuum representation of tumbled granular flows (Meier *et al.* 2007; Sturman *et al.* 2008). These granular flows and the non-inertial cylinder flow are particularly similar by sharing essential features: time-periodic flow composed of systematic reorientation of a base flow, spheroidal invariant surfaces and periodic lines of elliptic and hyperbolic type. Insight into the tracer dynamics subject to perturbations may, through these links with other systems, therefore contribute to further theoretical developments on generic three-dimensional Lagrangian transport and translation of fundamental knowledge into practical applications. In-depth investigation of the connection with other systems – and the generality of obtained results – is beyond the present scope, however.

5. Flow topology: response to weak inertial perturbations ($Re > 0$)

5.1. *Introduction*

Under inertial conditions, the fluid motion is governed by (2.1), with the Reynolds number Re controlling the strength of the inertial effects. Inertia introduces centrifugal forces to the momentum balance and thus causes the streamlines of the stepwise steady flows, shown in figure 3(*a*) for the first forcing step of the non-inertial limit $Re = 0$, to become open. This destroys the time-reversal reflectional symmetry of the individual forcing steps and, consequently, the time-reversal reflectional symmetries (4.2) and (4.5) of the forcing protocols considered here. Only the ordinary non-reflectional symmetry (4.3) of Protocol-$\mathscr{A}$' is preserved for $Re > 0$. This symmetry breaking brings about two fundamental changes in the flow topology: (i) the constant of motion vanishes and tracers are no longer restricted to the invariant surfaces shown in figure 7(*a*)

and (ii) the period-1 lines disclosed in § 4 transform into isolated period-1 points and the associated one-dimensional manifolds (Speetjens *et al.* 2006*a*). However, though strictly no longer present, the invariant surfaces and periodic lines dominate the dynamics in the limit of weak inertia through the so-called adiabatic behaviour in ways first investigated in Speetjens *et al.* (2006*a*,*b*) for Protocol-$\mathscr{A}$'. Hereafter, these investigations are expanded to Protocols-$\mathscr{A}$', $\mathscr{T}$ and $\mathscr{S}$ in order to demonstrate the generic nature of phenomena observed for Protocol-$\mathscr{A}$'. Moreover, the investigations on Protocols-$\mathscr{T}$ and $\mathscr{S}$ are to pave the way to future experimental studies on long-term three-dimensional tracer dynamics. These forcing protocols admit infinite repetition with a finite wall and thus can be realized in a laboratory set-up without restriction on the number of forcing cycles.

5.2. *Formation of adiabatic structures*

Coherent structures in the non-inertial flow topology may (partially) survive in an approximate manner under weak nonlinear perturbation (here, by inertia) on grounds of the so-called averaging principle (Arnold 1978). Such surviving structures are termed adiabatic structures. In the present context, adiabatic structures may emanate from both the invariant surfaces and the elliptic islands they hold.

The centrifugal forces set up a secondary motion transverse to the primary motion within the invariant surface and cause drifting of tracers transverse to this invariant surface. The drifting tracers occupy a shell of finite thickness that is centred upon the invariant surface of the non-inertial limit and gradually expands as time progresses. However, for sufficiently small $Re > 0$ this expansion is extremely slow, meaning that invariant surfaces approximately survive in the form of thin shells (constituting the corresponding adiabatic structures). The tracer remains confined to the thin adiabatic shell centred upon the original invariant surface for prolonged periods of time.

Closed orbits of the elliptic islands within adjacent invariant surfaces coalesce into concentric tubes centred upon the elliptic segments of the periodic line under weak nonlinear perturbation. Thus, elliptic tubes are formed as adiabatic counterpart to the elliptic islands (not shown). This happens in the same Re-range as that of formation of the adiabatic shells. Beyond this range, elliptic tubes disintegrate.

The above formation of elliptic tubes is in accordance with the transformation of two-action maps (tracers confined to invariant closed curves) into one-action maps (tracers confined to invariant tori) for arbitrarily small perturbations (Cartwright *et al.* 1996). The survival of (at least a subset of) invariant tori thus created, in turn, is in accordance with the three-dimensional counterpart to the well-known KAM theorem (Cheng & Sun 1990; Mezić & Wiggins 1994; Broer *et al.* 1996). Noteworthy to mention is that the elliptic tubes are finite, signifying incomplete invariant tori and thus implying that these theoretical predictions also hold true on a local level.

The formation of adiabatic shells and tubes basically occurs in all forcing protocols considered here. However, an essential dependence upon the forcing can be observed in that the Re-range accommodating adiabatic behaviour narrows significantly for more elaborate protocols; the typical range for the three-step Protocol-$\mathscr{T}$ and four-step Protocol-$\mathscr{S}$ is $Re \lesssim 0.01$ and $Re \lesssim 0.005$, respectively, compared to $Re \lesssim 0.1$ for the two-step Protocol-$\mathscr{A}$'. Furthermore, the adiabatic shells form only in regions where the underlying invariant surfaces accommodate chaotic advection; intra-surface regions with non-chaotic dynamics (e.g. elliptic islands and the direct proximity of cantori) result in holes in the adiabatic shells due to the local breakdown of the averaging principle. (In essence, a local competition between formation of an adiabatic shell and an elliptic tube takes place that is won by the tube formation due to the

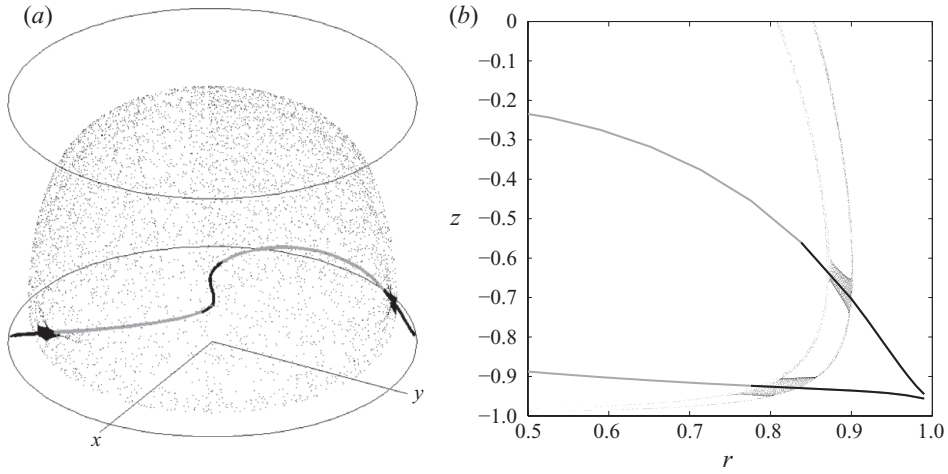

FIGURE 10. Formation of closed adiabatic structures in Protocol-$\mathscr{A}$' ($\theta_0 = \pi/3,\ D = 5$) by RIM ($Re = 0.1$) visualized by the Poincaré section of a single tracer. (*a*) Merger of elliptic tubes centred on outer elliptic segments of the period-1 line (curve; dark/bright indicate elliptic/hyperbolic segments) and adiabatic shells in perspective view and (*b*) close-up of the merger in the rz-projection.

fact that islands entrap tracers within subregions of the invariant shell and thus prevent such tracers to densely cover regions of the invariant surface.) Weak inertial perturbation thus creates multiple families of adiabatic structures, viz., the adiabatic shells corresponding with invariant surfaces and the families of concentric tubes corresponding with the elliptic segments of the periodic lines. However, these families, rather than coexisting, can interact. Such interaction and its effect upon the tracer dynamics is examined below.

5.3. *Merger of adiabatic structures in Protocol-$\mathscr{A}$'*

Previous studies on Protocol-$\mathscr{A}$' for $\theta_0 = \pi/2$ revealed that adiabatic shells and elliptic tubes may merge by a mechanism termed resonance-induced merger (RIM) (Speetjens *et al.* 2006*a*,*b*). RIM occurs near parabolic points (discriminant $\mathscr{D} = 0$ and eigenvalue spectrum $\boldsymbol{\Lambda} = \{1, 1, 1\}$; see § 3), where $\boldsymbol{\Phi}(\boldsymbol{x}) = \boldsymbol{x}$ not only holds for the period-1 point itself, but to good approximation also for its finite proximity. Thus, net motion ceases near the parabolic points in the Poincaré section; fluid elements – and thereby tracers – resonate near these points in the sense that they, similar to true period-1 points, return to their initial position after each cycle. This resonance results in breakdown of the averaging principle – and formation of holes in the adiabatic shells – specifically in those regions where families of elliptic tubes start or end. (Consult e.g. Vainchtein, Neishtadt & Mezić (2006) for a more detailed discussion on breakdown of the averaging principle by resonances.) This leads to the remarkable merger of tubes with adiabatic shells and the formation of intricate adiabatic structures. (The direct consequence of the segmentation of periodic lines.) Figure 10 demonstrates this for Protocol-$\mathscr{A}$' at $\theta_0 = \pi/3$ and $D = 5$ by way of the Poincaré section of a single tracer released in the direct proximity of the elliptic segment on the left and tracked forward and backward in time. This exposes the formation of fully closed adiabatic structures comprising two adiabatic shells connected by two elliptic tubes centred on the period-1 line by RIM. Two essential conditions underlie the formation of these particular adiabatic structures. First, chaotic advection within the associated invariant surfaces

everywhere outside the islands centred on the period-1 line. This ensures formation of complete adiabatic shells, save the holes that facilitate merger with the tubes. Second, the two intersections of the period-1 line with each invariant surface coincide with the elliptic segment of the period-1 line. This ensures occurrence of RIM – and thus merger with tubes – at both sides.

RIM occurring at both sides – and the above-mentioned formation of fully-closed adiabatic structures – is a direct consequence of the ordinary symmetry (4.3). The latter causes pairwise occurrence of period-1 points through

$$\boldsymbol{X}_1 = \boldsymbol{\Phi}(\boldsymbol{X}_1) \rightarrow \boldsymbol{X}_2 = \widetilde{S}(\boldsymbol{X}_1) = \boldsymbol{\Phi}(\boldsymbol{X}_2), \tag{5.1}$$

using $\widetilde{S}(\boldsymbol{X}_1) = \widetilde{S}\boldsymbol{\Phi}(\boldsymbol{X}_1) = \widetilde{S}\boldsymbol{\Phi}\widetilde{S}^{-1}\widetilde{S}(\boldsymbol{X}_1) = \boldsymbol{\Phi}\widetilde{S}(\boldsymbol{X}_1) = \boldsymbol{\Phi}(\boldsymbol{X}_2)$, with $\boldsymbol{X}_2$ being the image of $\boldsymbol{X}_1$ created by action of the symmetry operator $\widetilde{S}$. Moreover,

$$\widetilde{S}(\boldsymbol{X}_2) = \widetilde{S}^2(\boldsymbol{X}_1) = \boldsymbol{\Phi}(\boldsymbol{X}_1) = \boldsymbol{X}_1, \tag{5.2}$$

meaning that $\boldsymbol{X}_1$ is, in turn, the image of $\boldsymbol{X}_2$. These relations hold for any Re. In the non-inertial limit, $\boldsymbol{X}_1$ residing on the period-1 line in the symmetry plane (see e.g. figure 5*a*) implies that $\boldsymbol{X}_2$ must also reside in this plane – and thus on this line. Furthermore, in the non-inertial limit, the symmetry $\widetilde{S}$ (by virtue of the properties of its defining operators $S_{\theta_0/2}$ and $\boldsymbol{\Phi}_1$) maps material points only within an invariant surface, implying that $\boldsymbol{X}_{1,2}$ reside within the same invariant surface and thus identify with its two intersections by the period-1 line. Moreover, the pair $(\boldsymbol{X}_1, \boldsymbol{X}_2)$ is of the same type, that is, the associated deformation tensors according to (3.1) have identical eigenvalues,

$$\boldsymbol{F}_1 = \left.\frac{\partial \boldsymbol{\Phi}}{\partial \boldsymbol{x}}\right|_{\boldsymbol{X_1}} = \sum_{i=1}^{3} \lambda_i \boldsymbol{n}_i \boldsymbol{n}_i \rightarrow \boldsymbol{F}_2 = \left.\frac{\partial \boldsymbol{\Phi}}{\partial \boldsymbol{x}}\right|_{\boldsymbol{X_2}} = \sum_{i=1}^{3} \lambda_i \widetilde{S}(\boldsymbol{n}_i)\widetilde{S}^{-1}(\boldsymbol{n}_i), \tag{5.3}$$

with λ_i and $\boldsymbol{n}_i$ being the eigenvalues and eigenvectors, respectively, defined before. These symmetry-induced properties have the important implication that disconnected elliptic segments on the period-1 line, if existent, form interrelated pairs each of which intersect the same set of invariant surfaces in different regions. (The period-1 line in figure 5*a* e.g. contains two elliptic segments that form an interrelated pair.) RIM causes the tubes centred on the interrelated elliptic segments to connect with two adiabatic shells and form one closed adiabatic structure. This is demonstrated in figure 10 for $\theta_0 = \pi/3$, $D = 5$ and $Re = 0.1$. Figure 10(*a*) gives the perspective view on this newly formed structure and its position relative to the period-1 line (curve); figure 10(*b*) gives its projection in the rz-plane, clearly revealing the parts made up by the tubes and adiabatic shells. (Note the period-1 line contains three elliptic segments: two segments attached to the cylinder wall, forming an interrelated pair, and an isolated segment in the middle.) The ends of shown tubes centre on the elliptic segments, yet are relatively far away from the parabolic points bounding the elliptic segments (not indicated). These tubes are in fact part of a family of concentric tubes that become longer – and thus their ends progressively approach the bounding parabolic points – the smaller the diameter. The adiabatic behaviour demonstrated in figure 10 is the same as that observed for $\theta_0 = \pi/2$ in Speetjens *et al.* (2006*a*,*b*) and occurs in Protocol-$\mathscr{A}$' for any angle θ_0.

Essential difference with the case $\theta_0 = \pi/2$ studied before is the formation of the isolated elliptic segment in the middle of the period-1 line. This segment in fact comprises two sections separated by the stagnation point (intersection period-1 line with cylinder axis). The elliptic tubes emanating from this segment also exhibit RIM

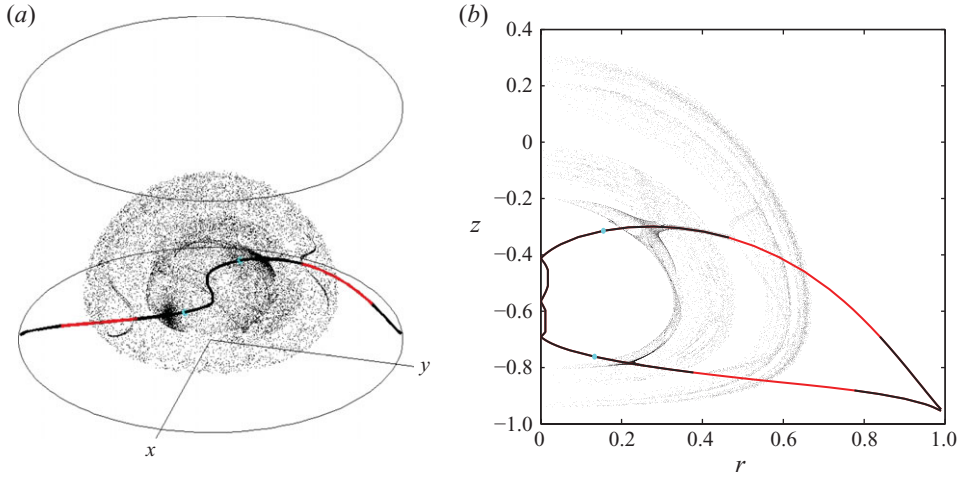

FIGURE 11. (Colour online) Formation of closed adiabatic structures in Protocol-$\mathscr{A}$' ($\theta_0 = \pi/6$, $D = 5$) by RIM ($Re = 0.1$) visualized by the Poincaré section of a single tracer. (*a*) Merger of elliptic tubes centred on the isolated elliptic segment of the period-1 line (curve; black/red indicate elliptic/hyperbolic segments) and adiabatic shells in perspective view and (*b*) rz-projection. Period-4 resonances are highlighted (cyan).

with adiabatic shells, yet in a somewhat different manner. This is demonstrated in figure 11 for $\theta_0 = \pi/6$, $D = 5$ and $Re = 0.1$. The outer tube ends, rather than connecting with shells, undergo bifurcation into pairs of period-2 tubes near the parabolic points separating the inner elliptic segment and the hyperbolic segments (red) on the period-1 line, as a result of the bifurcations in intra-surface dynamics with increasing r_s (similar to that demonstrated in figure 9 for Protocol-$\mathscr{T}$). These period-2 tubes are centred on period-2 lines (not shown) that intersect the period-1 line at the said parabolic points and connect with adiabatic shells via RIM. Moreover, these shells are leaky due to holes created by cantori outside their connecting region with the tubes. This leakiness facilitates random tracer exchange with the environment and switching between leaky shells, and thus creates the chaotic sea surrounding the adiabatic structure. The indirect RIM via bifurcating tubes and leakiness of adiabatic shells is in essence the same as that observed in Speetjens *et al.* (2006*a*) for period-2 tubes in the case $\theta_0 = \pi/2$. For generic cases of Protocol-$\mathscr{A}$' this may expose itself more elaborately owing to the larger variety in arrangement of islands in the underlying invariant surfaces.

The inner tube ends connect with an inner leaky shell through RIM also. However, here a new kind of resonance comes into play that is intimately related to the parabolic points underlying the above instances of RIM: period-1 points within elliptic segments with eigenvalue spectrum $\boldsymbol{\Lambda} = (1, i, -i)$ (discriminant $\mathscr{D} = -1$). These points, highlighted in cyan in figure 11, effectuate resonance every fourth mapping, i.e. $\boldsymbol{\Phi}^4(\boldsymbol{x}) \approx \boldsymbol{x}$ in their direct vicinity, and may thus be considered a somewhat weaker variant of the periodwise resonance $\boldsymbol{\Phi}(\boldsymbol{x}) \approx \boldsymbol{x}$ near parabolic points ($\mathscr{D} = 0$). The resonances associated with $\mathscr{D} = -1$ are termed period-4 resonances hereafter.

The period-4 resonances, since the corresponding value of the discriminant $\mathscr{D} = -1$ cannot be determined exactly in numerical search algorithms, are associated with those period-1 points that meet $|D + 1| \leqslant \epsilon$, with $\epsilon \ll 1$. (At parabolic points separating elliptic and hyperbolic segments, on the other hand, $\mathscr{D}$ always changes

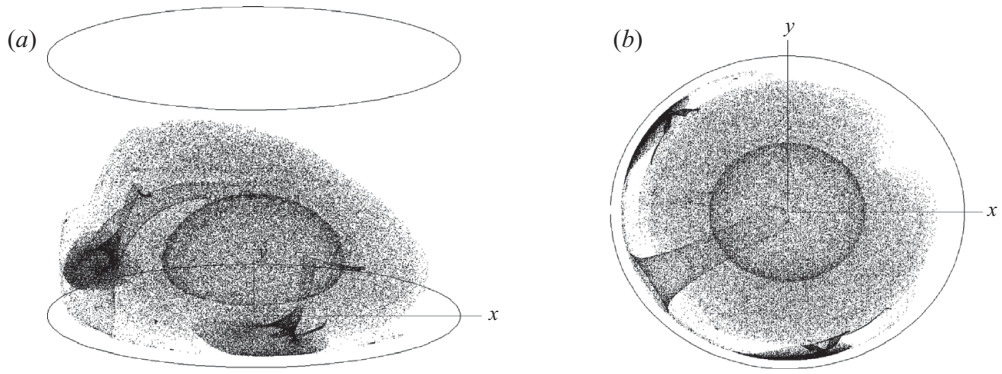

FIGURE 12. Formation of adiabatic structures in Protocol-$\mathscr{T}$ ($D = 14$) by RIM ($Re = 0.01$) visualized by the Poincaré section of a single tracer. (a) Perspective view and (b) top view.

sign, meaning these points admit accurate and reliable numerical isolation.) Hence, the period-4 resonances may emerge as narrow segments instead of isolated points in the numerical results. Note that this in fact is consistent with the approximate nature of the averaging principle.

5.4. *Merger of adiabatic structures in Protocol-$\mathscr{T}$*

The closed protocols exhibit in essence similar behaviour as found for Protocol-$\mathscr{A}$' in that merger between tubes and shells also occurs via RIM. Figure 12 gives a typical situation for Protocol-$\mathscr{T}$ at $D = 14$ and $Re = 0.01$. Clearly distinguishable are coherent structures comprising tubes and adiabatic shells embedded in a chaotic environment. However, despite this resemblance, manifestations of RIM are considerably more diverse compared to the above cases (in part) due to a fundamental difference with Protocol-$\mathscr{A}$', namely the absence of an ordinary symmetry as (4.3). This enlarges the geometrical freedom of coherent structures in that shell-tube connections must no longer emerge pairwise and may also occur isolated. An important quantitative difference is the significantly stronger variation in intra-surface dynamics relative to Protocol-$\mathscr{A}$'. These differences admit greater dynamical richness. This is demonstrated below.

Considered is RIM associated with the period-1 line for Protocol-$\mathscr{T}$ at $D = 14$ and $Re = 0.01$, shown in figure 6(c), accommodating elliptic and hyperbolic segments as indicated. Besides the parabolic points separating the latter segments, isolated period-4 resonances as discussed above, as well as an essentially similar kind, occur: isolated period-1 parabolic points within elliptic segments (denoted isolated period-1 resonances in the following). Figure 13(a) shows the period-1 line including the isolated period-1 (blue) and period-4 (cyan) resonances, clearly revealing the considerably more complex segmentation of the period-1 line compared to those of Protocol-$\mathscr{A}$'.

The isolated resonances trigger RIM in essentially the same way as before. This is demonstrated in figures 13(b–d) by means of the Poincaré section of a tracer released near the isolated period-1 resonance just below the midplane $z = 0$. The projection in the rz-plane exposes the merger of an elliptic tube centred on the elliptic segment between the isolated period-1 resonance and the cylinder wall with an inner and outer adiabatic shell in a similar manner as shown in figure 10 for Protocol-$\mathscr{A}$'. This tube belongs to the same family as that extending from the upper part of the inner adiabatic shell outlined in figure 12(a). The outer adiabatic shell in figure 13 forms

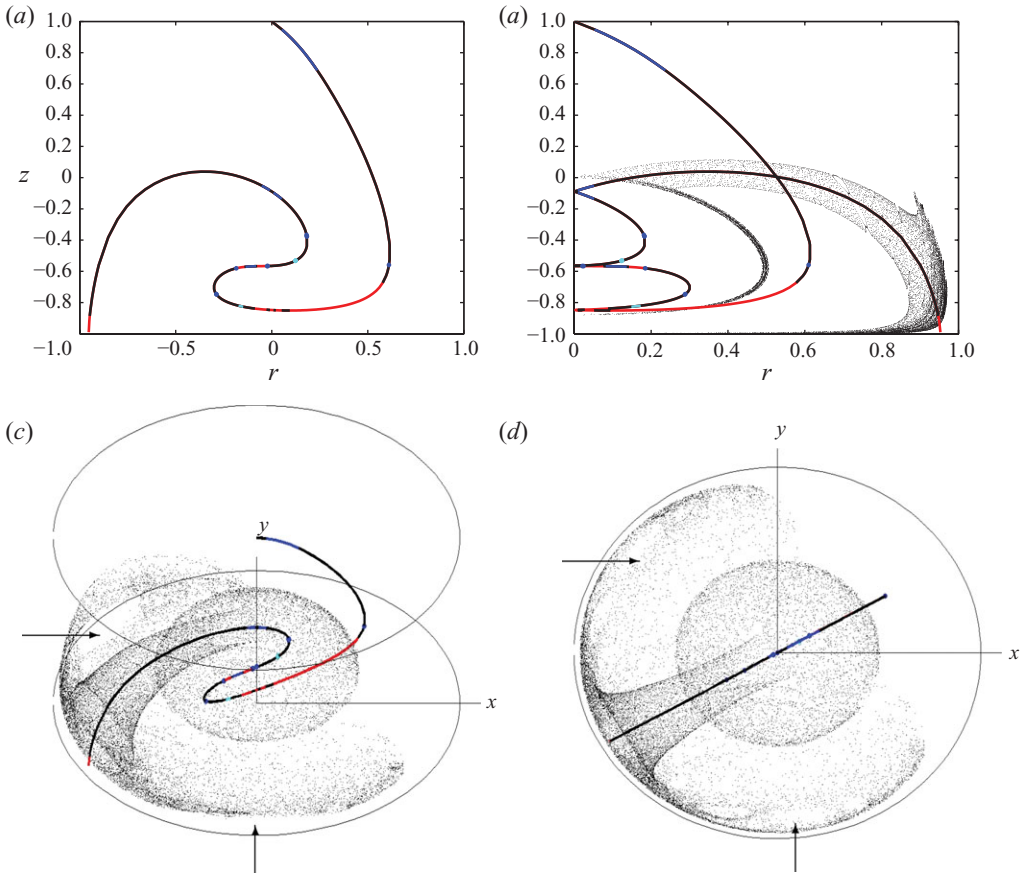

FIGURE 13. (Colour online) Formation of adiabatic structures in Protocol-$\mathscr{T}$ ($D = 14$) by RIM ($Re = 0.01$) due to isolated period-1 resonances visualized by the Poincaré section of a single tracer. (*a*) Period-1 line with elliptic (black) and hyperbolic (red) segments and isolated period-1 (blue) and period-4 (cyan) resonances as indicated, (*b*) rz-projection of adiabatic structure, (*c*) perspective view of adiabatic structure and (*d*) top view of adiabatic structure. Arrows indicate holes in outer shell due to higher-order elliptic tubes.

only in the lower region near the bottom wall due to the large island covering the upper part of the associated invariant surfaces near the solid walls and, furthermore, has sizeable holes (indicated by arrows) resulting from the higher-order islands in the bottom-wall region (figure 9*f*). (The latter islands merge into the elliptic tubes arranged symmetrically about the symmetry plane in figure 12.) The incompleteness of the outer shell enables random tracer exchange with the environment, similar to that observed before for Protocol-$\mathscr{A}$', and contributes to the formation of the chaotic sea enveloping the adiabatic structures in figure 12.

Figure 14(*a*) shows a companion structure of that in figure 13. Principal difference with the latter is that here the outer adiabatic shell, instead of being incomplete and leaking tracers into the chaotic sea, merges with a large elliptic tube emanating from the beforementioned large islands covering the outer invariant surfaces. This large tube, in turn, reattaches to an inner adiabatic shell via RIM at the isolated period-1 resonance near the right deflection point that approximately coincides with the inner shell corresponding with the narrow tube. This is demonstrated in figure 14(*b–d*). The

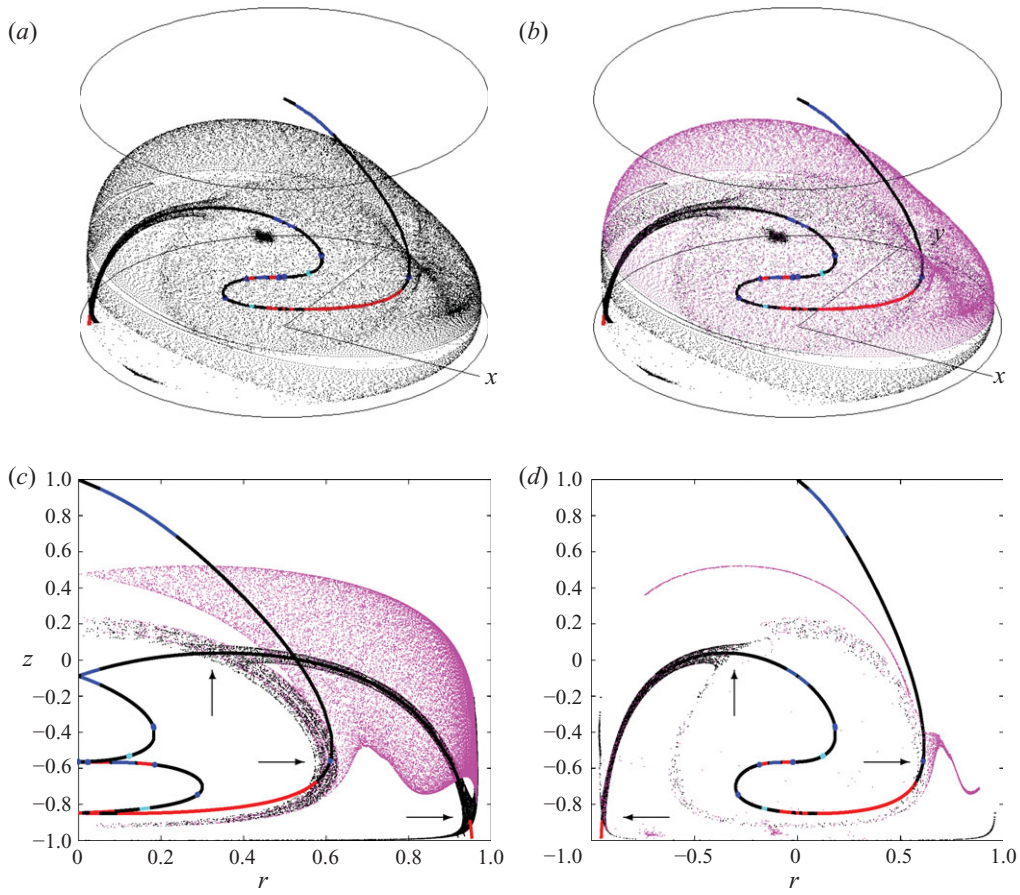

FIGURE 14. Formation of adiabatic structures in Protocol-$\mathscr{T}$ ($D=14$) by RIM ($Re=0.01$) due to isolated period-1 resonances visualized by the Poincaré section of a single tracer: (a) perspective view of entire adiabatic structure; (b) perspective view of adiabatic structure with large tube and inner shell highlighted; (c) rz-projection of adiabatic structure; (d) portion of adiabatic structure in slice of thickness $\delta=0.1$ centred on symmetry plane. The period-1 line (curve) is included with elliptic (black) and hyperbolic (red) segments and isolated period-1 (blue) and period-4 (cyan) resonances as indicated. Arrows indicate instances of RIM.

colour-coding of the period-1 line is as before. Black tracers visualize the narrow tube and its associated inner and outer adiabatic shells; coloured tracers visualize the large tube and the inner shell to which it connects. (Recall that shown points correspond to the Poincaré section of a single physical tracer.) Figure 14(b) reveals the transition from outer shell into the large tube via the gap separating the black and coloured regions. (This gap coincides with the transition from chaotic region to the elliptic islands in figure 9f.) Important to note is that, though an adiabatic shell and an elliptic tube connect here, RIM due to the period-1 line is not the underlying mechanism here. Figure 14(c) (rz-projection) and figure 14(d) (slice of thickness $\delta=0.1$ centred on symmetry plane) expose the three instances of RIM (indicated by arrows) by which the adiabatic shells and tubes merge into one adiabatic structure. However, despite the formation of a complete structure, tracer exchange with the environment nonetheless occurs via the relatively ill-defined (and therefore leaky) inner shells. Moreover, these inner shells must, contrary to Protocol-$\mathscr{A}$', not necessarily emanate from the same

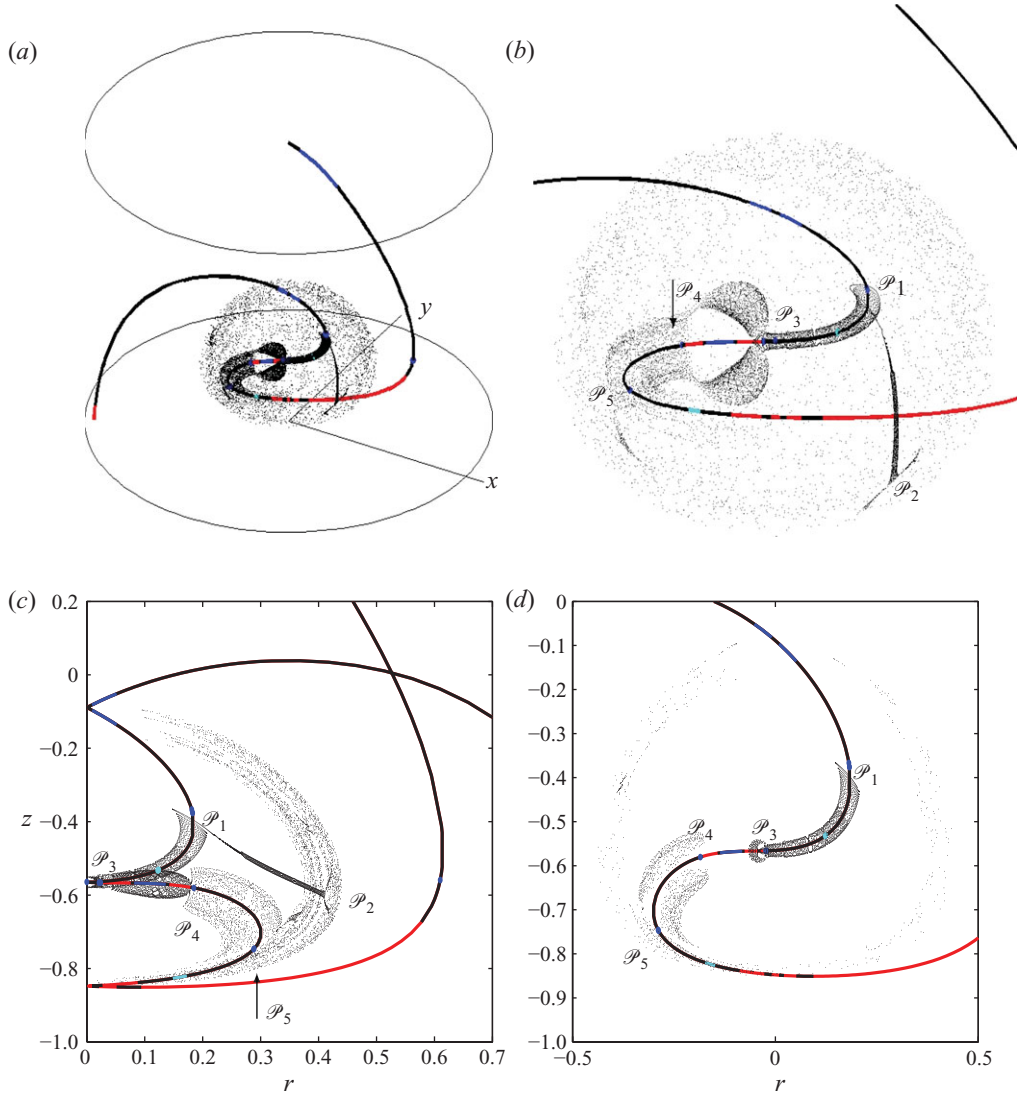

FIGURE 15. Formation of adiabatic structures in Protocol-$\mathscr{T}$ ($D = 14$) in the interior region ($Re = 0.01$) visualized by the Poincaré section of a single tracer (magenta star indicates initial position). (*a*) Perspective view, (*b*) close-up of the perspective view, (*c*) rz-projection and (*d*) close-up of slice of thickness $\delta = 0.1$ centred on symmetry plane. The period-1 line (curve) is shown by elliptic (black) and hyperbolic (red) segments, with isolated period-1 (blue) and period-4 (cyan) resonances as indicated. Symbols point out features as explained in the text.

invariant surface on grounds of the absence of a symmetry of the type (4.3). This may further promote leakage via the inner shells. The dynamics within the interior of the domain enclosed by the above adiabatic structures is of even greater richness due to the intricate segmentation of the period-1 line (figure 13*a*) in this region. However, RIM(-like) behaviour plays an essential role here as well. Figure 15(*c*) demonstrates this for the structures visualized by a single tracer released in the proximity of the period-1 line at the position indicated by the magenta star in panel. Regression in time causes upward migration via an elliptic tube towards the isolated

period-1 resonance $\mathscr{P}_1$. Here, bifurcation into a higher-order tube occurs that, in turn, undergoes bifurcation into two higher-order tubes that attach to an outer adiabatic shell in the region $\mathscr{P}_2$. Thus, the period-1 tube connects through bifurcations with the outer shell via indirect RIM akin to that observed before for Protocol-$\mathscr{A}$' (figure 11). Progression in time causes downward migration of the tracer by the same elliptic tube as before towards the isolated period-1 resonances at $\mathscr{P}_3$. (Note that, somewhat surprisingly, the tube is unaffected by the isolated period-4 resonance it encloses. This suggests its effect on the dynamics is too weak or too localized to prevent continuation of the tube. Further investigation is beyond the present scope, however.) Here, the elliptic tube bifurcates into two higher-order tubes that envelop a hyperbolic segment on the period-1 line containing period-1 resonances before merging into a single elliptic tube again (signifying a reversed bifurcation) at the two isolated period-1 resonances sitting at $\mathscr{P}_4$. This tube attaches via RIM to the beforementioned outer adiabatic shell near the period-1 resonance $\mathscr{P}_5$. Thus, an adiabatic structure is formed that comprises an intricate arrangement of interconnected (higher-order) tubes that connects two regions of a leaky adiabatic shell. (The lower period-4 resonance in fact coincides with this shell and thus contributes to its leakiness.) This structure exchanges material with the environment through the latter shell. These observations for the interior of the domain lift but a tip of the veil of the complex dynamics taking place in this region. Further investigation is beyond the present scope and is to be the subject of future studies.

5.5. *Merger of adiabatic structures: generalization*

The adiabatic behaviour discussed above generalizes to Protocol-$\mathscr{T}$ for other displacements D and Protocol-$\mathscr{S}$ in that segmentation of periodic lines results in interactions and merger of coherent structures – and thus formation of adiabatic structures – in ways qualitatively similar to that demonstrated in figures 12–15. However, in quantitative sense, behaviour may generally exhibit substantial diversity, consistent with the great variation in intra-surface dynamics as a function of displacement D and radius r_s, as illustrated for Protocol-$\mathscr{T}$ in figures 8 and 9, respectively.

First instances of adiabatic behaviour for Protocol-$\mathscr{S}$ are given in figure 16 for $D=10$ and $Re=0.005$ by way of the Poincaré section of a single tracer released in the proximity of an elliptic segment of the period-1 line. This exposes several coherent structures, of which one is directly connected with the period-1 line, namely the large period-1 tube and adiabatic outer shell highlighted in figures 16(b)–(d). The period-1 line exhibits segmentation into elliptic and hyperbolic sections and period-1/period-4 resonances in a comparably intricate manner as found before for Protocol-$\mathscr{T}$. The merger of the outer end of the period-1 tube and the adiabatic shell is, similar to the behaviour observed for Protocol-$\mathscr{A}$' at $\theta_0=\pi/6$, $D=5$ and $Re=0.1$ (figure 11), triggered by RIM due to an isolated period-4 resonance. The inner end of the period-1 tube undergoes bifurcation into a higher-order tube rather than the typical merger with an inner adiabatic shell found in the previous cases. This prevalence of tube bifurcations over tube-shell merger, reminiscent of the dynamics in the inner regions of Protocol-$\mathscr{T}$ (figure 15), is believed to result directly from the intricate intra-surface dynamics – reflected in the arrangements of elliptic islands – of the underlying invariant surfaces (as e.g. demonstrated in figure 7b) and the inherent complex segmentation of the period-1 line. The rz-projection in figure 16(d), in particular, offers first insight into the immense complexity of the adiabatic structures

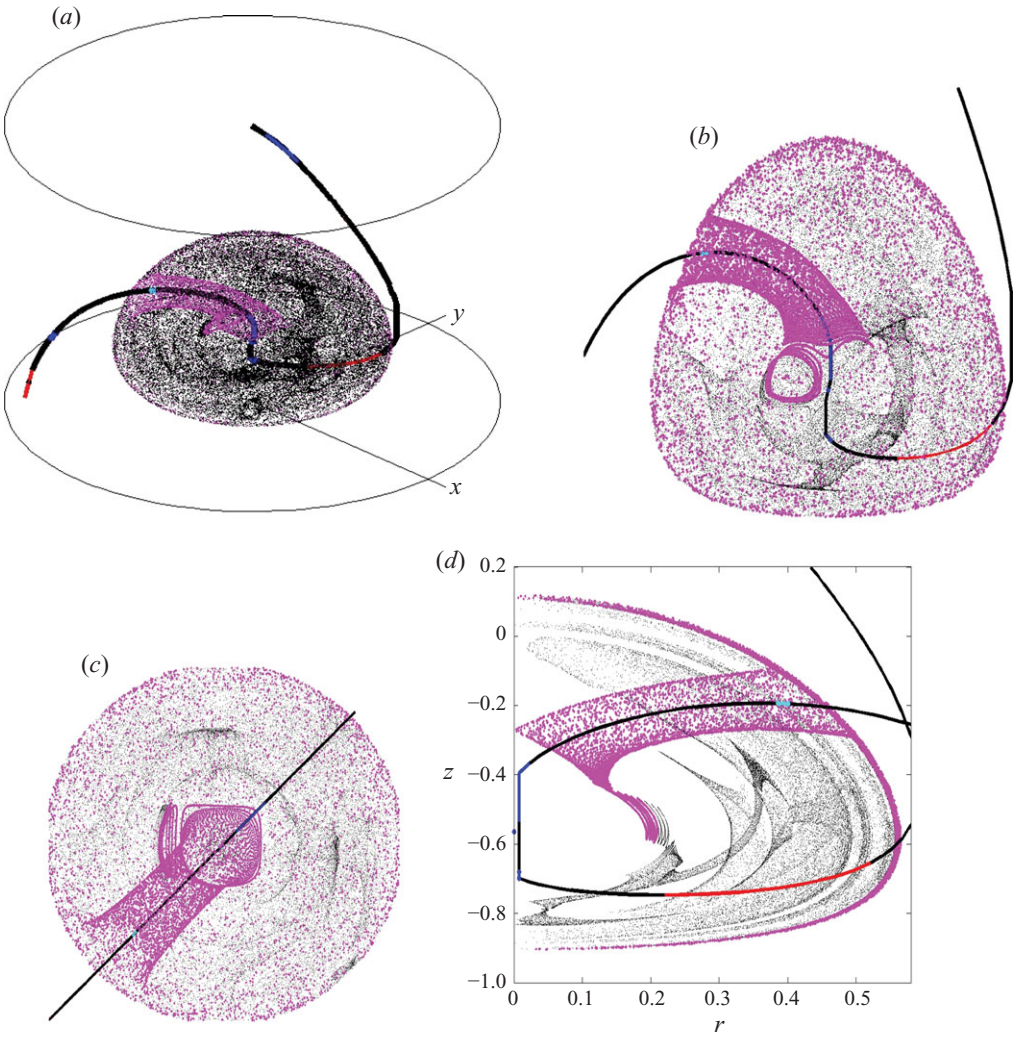

FIGURE 16. Formation of adiabatic structures in Protocol-$\mathscr{S}$ ($D = 10$) for $Re = 0.005$ visualized by the Poincaré section of a single tracer. (*a*) Perspective view, (*b*) close-up perspective view, (*c*) top view and (*d*) rz-projection. The highlighted adiabatic structure (magenta) comprises a period-1 tube and outer shell merged by RIM. The period-1 line (curve) is shown by elliptic (black) and hyperbolic (red) segments, with isolated period-1 (blue) and period-4 (cyan) resonances as indicated.

formed by such bifurcations. Further investigation of these phenomena is the subject of ongoing studies.

5.6. *Outlook to laboratory experiments*

To date the adiabatic behaviour (and then, in particular, RIM) inside the cylinder flow has been investigated only through numerical simulations. This behaviour is of great importance for three-dimensional mixing flows by, first, providing new fundamental insight into the transport dynamics of three-dimensional unsteady flows (consisting of piecewise steady flows) and, second, by potentially offering ways for methodical manipulation of these transport properties for mixing purposes.

	Simulations		Experiments		
Protocol	Re	D	U (cm s^{-1})	D_w (cm)	T (s)
$\mathscr{T}$	0.01	14	5	28	16.8
$\mathscr{S}$	0.005	10	2.5	20	32

TABLE 1. Design parameters for laboratory experiments on the closed forcing protocols.

Laboratory experiments on this adiabatic behaviour are imperative for bridging the gap to (future) mixing applications. The closed forcing protocols (i.e. Protocols-$\mathscr{T}$ and $\mathscr{S}$) admit long-term experiments with finite walls and thus are to serve as model flows to be investigated in future laboratory experiments. First aims are validation of key features of both the non-inertial limit (invariant surfaces, periodic lines, intra-surface dynamics) and the corresponding adiabatic state (formation of tubes and shells, tube-shell connections). These prospective experiments expand on the exploratory experiments on the non-inertial baseline flow in Speetjens *et al.* (2004) and are to employ the following experimental techniques: laser-induced fluorescence (LIF) for visualization of coherent structures based on the course of action by Fountain, Khakhar & Ottino (1998) and Fountain *et al.* (2000) and three-dimensional particle-tracking velocimetry (3DPTV) for measurement of three-dimensional Lagrangian fluid trajectories and three-dimensional velocity fields employing the methodology by Luethi, Tsinober & Kinzelbach (2005). LIF is, on grounds of its limited spatial resolution relative to 3DPTV, to be employed for visualization of large(r)-scale features; 3DPTV is to be employed primarily for detailed isolation of intra-surface topologies and adiabatic structures and especially the delicate small-scale features related to RIM. Hence, the 3DPTV experiments will be the most challenging and therefore will serve as guidance for a first estimate of design and operating parameters. This is elaborated below.

Relevant parameters are the wall velocity U, wall-displacement D_w and the duration of one forcing period T that, through definitions $Re = UR/\nu$ and $D = D_w/R = UT/nR$, relate to the non-dimensional system parameters via $U = Re\,\nu/R$, $D_w = DR$ and $T = nD_w/U = nDR^2/Re\,\nu$. Parameters D_w and T are of particular importance in that both determine the scale of the laboratory set-up and the duration of the measurements, respectively. Presuming, similar to the laboratory set-up of Speetjens *et al.* (2004), a cylinder radius of the order of a few centimetres and a high-viscosity silicon oil (offered by Wacker GmbH, Germany in the viscosity range $10^{-6} - 1\,\mathrm{m^2\,s^{-1}}$), yields estimates for the experimental settings corresponding with the closed protocols considered in the present study, according to table 1. These estimates are based on $R = 2\,\mathrm{cm}$ and $\nu = 0.1\,\mathrm{m^2\,s^{-1}}$ and the constraint $U \leqslant 5\,\mathrm{cm\,s^{-1}}$ set by a maximally allowable wall acceleration during change of direction. (The (de-)acceleration stages involved with switching between forcing steps become longer with higher translation velocity due to the inertia of the wall, causing growing departure from the piecewise steady wall translation. Test runs indicated that these stages are negligible – and the piecewise steady nature of the flow upheld – for the given velocity constraint.) Note that condition $T_\nu/T_{step} \sim O(10^{-4}) \ll 1$ for ensuring piecewise steady motion is well met (§ 2). RIM occurs for very small departures from the Stokes limit, i.e. typically $Re \sim O(10^{-2})$, meaning that accurate control of Re is critical for reliable performance of laboratory experiments. The variation in set translation velocity is $\Delta U \sim O(0.1\,\mathrm{mm\,s^{-1}})$, implying a sufficient absolute accuracy

$\Delta Re = \Delta U R/\nu \sim O(10^{-5})$ in the Reynolds number. Important to recall is that, on account of the numerical method, physical Reynolds numbers are an estimated factor two lower compared to those considered in the present study (§ 2.2). This can be readily adjusted for via the fluid viscosity and thus is of no consequence to the above.

These estimates imply length and velocity scales that are easily realizable in a laboratory set-up. However, given that visualization of (topological features within) invariant surfaces and adiabatic structures with 3DPTV may require hundreds of forcing periods, direct measurement of Poincaré sections involves continuous 3DPTV measurements with durations of the order of hours and thus is a challenging objective. An alternative to this direct Lagrangian approach may be found in a hybrid numerical–experimental course of action similar to that pursued by Voth, Haller & Gollub (2002) for two-dimensional chaotic flows. The latter evaluate long-term Lagrangian quantities by numerical tracking of tracer motion employing a two-dimensional velocity field obtained through high-resolution velocimetry. The present configuration admits a similar approach based on accurate 3DPTV velocity measurements of the steady base flow underlying the forcing protocols (§ 4) by the methodology of Luethi *et al.* (2005). Resolution of this three-dimensional base flow may be augmented further by combining data obtained for consecutive time steps into one overall flow field. Design and realization of these laboratory experiments is currently underway.

6. Conclusions

The present study concerns the role of fluid inertia (parameterized by the Reynolds number Re) in the three-dimensional advection properties of passive tracers inside a cylinder flow driven by time-periodic motion of one endwall. Tracer advection is studied in a Lagrangian framework by examining the topological properties of the coherent structures that form in the three-dimensional web of tracer paths. Such coherent structures geometrically determine the transport properties of the flow. Primary goal is further exploration of a recently disclosed fundamental transport phenomenon: the merger of coherent structures formed in the non-inertial limit ($Re = 0$) into intricate new structures embedded in chaotic regions by a mechanism termed resonance-induced merger (RIM) triggered by weak fluid inertia ($Re > 0$). Two key issues are addressed: (i) establishing the degree of universality of RIM and (ii) paving the way to experimental investigation of RIM. To these ends RIM has been examined in a number of cylinder flows. The following conclusions can be reached.

RIM has been observed in all flow configurations examined. Key ingredients are adiabatic shells and elliptic tubes emanating from weak inertial perturbation of the spheroidal invariant surfaces and elliptic islands within these surfaces, respectively, of the non-inertial limit. Merger of adiabatic shells and elliptic tubes by RIM, consistent with previous studies, ensued from resonances located on the elliptic segments of the periodic lines. This strongly suggests that RIM is indeed a universal phenomenon and key to an essentially three-dimensional route to chaos.

Part of the resonances stems from parabolic points that separate elliptic and hyperbolic segments on the periodic lines; this type has been encountered before. The present study isolated two further types of resonance that cause RIM: (i) isolated parabolic points inside elliptic segments of periodic lines and (ii) period-4 resonances (i.e. occurring after four cycles instead of one) inside these segments. This strongly

suggests that RIM may, in principle, originate from any period-p resonance, with $p \geqslant 1$, located on any (higher-order) periodic line inside the system.

The occurrence of RIM itself is essentially equivalent in all flows considered. However, its manifestation in tracer dynamics varies significantly with the particular flow due to the great diversity in the underlying non-inertial states. The general trend is that the topology and arrangement of adiabatic structures formed by RIM grow more complex with increasing convolution and segmentation of periodic lines. Thus, multiple families of adiabatic structures can be formed that together define an intricate network of (intertwined) coherent structures embedded in chaotic seas. Structures may spatially confine tracers, yet may also exchange material with chaotic seas – and thus, indirectly with other structures. This brings about an enormous richness of three-dimensional tracer dynamics.

The above findings substantiate the important hypothesis that RIM is a universal phenomenon that occurs in any three-dimensional time-periodic flow accommodating invariant surfaces topologically equivalent to spheroids and (higher-order) periodic lines with segmentation into elliptic and hyperbolic sections. They furthermore provide strong evidence that RIM is a key element in an essentially three-dimensional route to global chaos in flows of this generic topological make-up. Further theoretical and numerical investigations on RIM in particular – and inertia-induced transport phenomena in general – by means of the cylinder flow are in progress. Investigations of resonances underlying RIM may hinge on methods by Litvak-Hinenzon & Rom-Kedar (2002) and Vainchtein *et al.* (2006). Topological analyses, in general, may benefit greatly from the recent Lagrangian techniques by Branicki & Wiggins (2009) developed specifically for three-dimensional unsteady systems.

The considered cylinder flows in part concern the so-called closed forcing protocols (i.e. zero net wall displacement during one cycle) that admit unrestricted repetition with a finite-size endwall. These configurations – and the simulated dynamics presented here – serve as a blueprint for laboratory experiments on three-dimensional transport phenomena. This is a major (future) research objective and realization of such experiments is currently underway.

The non-inertial limits of the cylinder flows furthermore closely relate to other systems considered in literature: volume-preserving systems with invariant surfaces in general (Mezić & Wiggins 1994; Gómez & Meiss 2002; Mullowney *et al.* 2008) and tumbled granular flows in particular (Meier *et al.* 2007; Sturman *et al.* 2008). Hence, present and future insight gained into the dynamics of the (perturbed) cylinder flows – and its reconciliation with the said systems – is potentially relevant to further development of a generic theoretical framework for three-dimensional unsteady transport as well as its application to realistic transport problems. Future research is planned to further explore these issues.

Z. Pouransari gratefully acknowledges financial support from the Dutch Foundation for Fundamental Research on Matter (FOM).

REFERENCES

Aref, H. 2002 The development of chaotic advection. *Phys. Fluids* **14**, 1315–1325.

Arnold, V. I. 1978 *Mathematical Methods of Classical Mechanics*. Springer.

Bajer, K. 1994 Hamiltonian formulation of the equations of streamlines in three-dimensional steady flows. *Chaos Solitons Fractals* **4**, 895–911.

Beebe, D. J., Mensing, G. A. & Walker, G. M. 2002 Physics and applications of microfluidics in biology. *Annu. Rev. Biomed. Engng* **4**, 261.

Bertsch, A., Heimgartner, S., Cousseau, P. & Renaud, P. 2001 Static micromixers based on large-scale industrial mixer geometry. *Lab Chip* **1**, 56.

Branicki, M. & Wiggins, S. 2009 An adaptive method for computing invariant manifolds in non-autonomous, three-dimensional dynamical systems. *Physica* D **238**, 1625.

Broer, H. W., Huitema, G. B. & Sevryuk, M. B. 1996 *Quasi-periodic Motions in Families of Dynamical Systems: Order Amidst Chaos*. Springer.

Cartwright, J. H. E., Feingold, M. & Piro, O. 1996 Chaotic advection in three-dimensional unsteady incompressible laminar flow. *J. Fluid Mech.* **316**, 259–284.

Cheng, C. Q. & Sun, Y. S. 1990 Existence of invariant tori in three-dimensional measure preserving mappings. *Celest. Mech.* **47**, 275–292.

Fountain, G. O., Khakhar, D. V., Mezić, I. & Ottino, J. M. 2000 Chaotic mixing in a bounded three-dimensional flow. *J. Fluid Mech.* **417**, 265–301.

Fountain, G. O., Khakhar, D. V. & Ottino, J. M. 1998 Chaotic mixing in a bounded three-dimensional flow. *Science* **281**, 683–686.

Franjione, J. G., Leong, C.-W. & Ottino, J. M. 1989 Symmetries within chaos: a route to effective mixing. *Phys. Fluids* A **11**, 1772–1783.

Gómez, A. & Meiss, J. D. 2002 Volume-preserving maps with an invariant. *Chaos* **12**, 289.

Jaluria, Y. 2003 Thermal processing of materials: from basic research to engineering. *ASME J. Heat Transfer* **125**, 957.

Litvak-Hinenzon, A. & Rom-Kedar, V. 2002 Parabolic resonances in 3 degree of freedom near-integrable Hamiltonian systems. *Physica* D **164**, 213.

Luethi, B., Tsinober, A. & Kinzelbach, W. 2005 Lagrangian measurement of vorticity dynamics in turbulent flow. *J. Fluid Mech.* **528**, 87.

MacKay, R. S. 1994 Transport in 3d volume-preserving flows. *J. Nonlinear Sci.* **4**, 329–354.

Malyuga, V. S., Meleshko, V. V., Speetjens, M. F. M., Clercx, H. J. H. & van Heijst, G. J. F. 2002 Mixing in the stokes flow in a cylindrical container. *Proc. R. Soc. Lond.* A **458**, 1867–1885.

Meagher, R. J., Hatch, A. V., F.Renzi, R. & Singh, A. K. 2008 An integrated microfluidic platform for sensitive and rapid detection of biological toxins. *Lab Chip* **8**, 2046.

Meier, S. W., Lueptow, R. M. & Ottino, J. M. 2007 A dynamical systems approach to mixing and segregation of granular materials in tumblers. *Adv. Phys.* **56**, 757–827.

Meleshko, V. V. & Peters, G. W. M. 1996 Periodic points for two-dimensional stokes flow in a rectangular cavity. *Phys. Lett.* A **216**, 87–96.

Mezić, I. 2001 Break-up of invariant surfaces in action-angle-angle maps and flows. *Physica* D **154**, 51.

Mezić, I. & Wiggins, S. 1994 On the integrability and perturbation of three-dimensional fluid flows with symmetry. *J. Nonlinear Sci.* **4**, 157–194.

Mullowney, P., Julien, K. & Meiss, J. D. 2008 Chaotic advection and the emergence of tori in the Küppers–Lortz state. *Chaos* **18**, 033104.

Nguyen, N.-T. & Wu, Z. 2005 Micro-mixers – a review. *J. Micromech. Microengng* **15**, R1.

Ott, E. 1993 *Chaos in Dynamical Systems*. Cambridge University Press.

Ottino, J. M. 1989 *The Kinematic of Mixing: Stretching, Chaos and Transport*. Cambridge University Press.

Ottino, J. M., Jana, S. C. & Chakravarthy, V. S. 1994 From Reynolds's stretching and folding to mixing studies using horseshoe maps. *Phys. Fluids* **6**, 685–699.

Ottino, J. M. & Wiggins, S. 2004 Introduction: mixing in microfluidics. *Phil. Trans. R. Soc. Lond.* A **362**, 923.

Shankar, P. N. 1997 Three-dimensional eddy structure in a cylindrical container. *J. Fluid Mech.* **342**, 97–118.

Speetjens, M. F. M. 2001 *Three-Dimensional Chaotic Advection in a Cylindrical Domain*. PhD thesis, Eindhoven University of Technology.

Speetjens, M. F. M. & Clercx, H. J. H. 2005 A spectral solver for the Navier–Stokes equations in the velocity-vorticity formulation. *Intl J. Comput. Fluid Dyn.* **19**, 191–209.

Speetjens, M. F. M., Clercx, H. J. H. & van Heijst, G. J. F. 2004 A numerical and experimental study on advection in three-dimensional stokes flows. *J. Fluid Mech.* **514**, 77–105.

Speetjens, M. F. M., Clercx, H. J. H. & van Heijst, G. J. F. 2006*a* Inertia-induced coherent structures in a time-periodic viscous mixing flow. *Phys. Fluids* **18**, 083603.

Speetjens, M. F. M., Clercx, H. J. H. & van Heijst, G. J. F. 2006*b* Merger of coherent structures in time-periodic viscous flows. *Chaos* **16**, 0431104.

Speetjens, M., Metcalfe, G. & Rudman, M. 2006*c* Topological mixing study of non-Newtonian duct flows. *Phys.* Fluids **18**, 103103.

Squires, T. M. & Quake, S. R. 2005 Microfluidics: fluid physics at the nanoliter scale. *Rev. Mod. Phys.* **77**, 977.

Stone, H. A., Stroock, A. D. & Ajdari, A. 2004 Engineering flows in small devices: microfluidics toward a lab-on-a-chip. *Annu. Rev. Fluid Mech.* **36**, 381.

Sturman, R., Meier, S. W., Ottino, J. M. & Wiggins, S. 2008 Linked twist map formalism in two and three dimensions applied to mixing in tumbled granular flows. *J. Fluid Mech.* **602**, 129–174.

Sturman, R., Ottino, J. M. & Wiggins, S. 2006 *The Mathematical Foundations of Mixing*. In *Cambridge Monographs on Appl. and comp. Math.* **22**, Cambridge University Press.

Sunden, B. & Shah, R. K. 2007 *Advances in Compact Heat Exchangers.* Springer.

Tourovskaia, A., Figueroa-Masot, X. & Folch, A. 2005 Differentiation-on-a-chip: a microfluidic platform for long-term cell culture studies. *Lab Chip* **5**, 14.

Vainchtein, D. L., Neishtadt, A. I. & Mezić, I. 2006 On passage through resonances in volume-preserving systems. *Chaos* **16**, 043123.

Voth, G. A., Haller, G. & Gollub, J. P. 2002 Experimental measurements of stretching fields in fluid mixing. *Phys. Rev. Lett.* **88**, 254501.

Weigl, B., Labarre, G., Domingo P. & Gerlach, J. 2008 Towards non- and minimally instrumented, microfluidics-based diagnostic devices. *Lab Chip* **8**, 1999.

Wiggins, S. & Ottino, J. M. 2004 Foundations of chaotic mixing. *Phil. Trans. R. Soc. Lond.* A **362**, 937.